JGR Oceans

Key Points:

- Annual maximum fast ice and sub-ice platelet layer thickness distributions are surveyed by airborne electromagnetics over 700 km of Ross Sea
- Deformed against the coast, 50% of transect volume was rough first-year fast ice (mode 3.3 m thick), that was thicker than nearby pack ice
- Sub-ice platelet layers over 0.5 m thick underlay level ice over large parts of four embayments, revealing land ice-fast ice interaction

Supporting Information:

Supporting Information may be found in the online version of this article.

Correspondence to:

P. J. Langhorne,
pat.langhorne@otago.ac.nz

Author Contributions:

Conceptualization: P. J. Langhorne, C. Haas, D. Price, W. Rack, G. M. Brett
Data curation: P. J. Langhorne
Formal analysis: P. J. Langhorne, D. Price, G. H. Leonard, S. Urbini
Funding acquisition: P. J. Langhorne, C. Haas, D. Price, W. Rack, G. M. Brett
Investigation: C. Haas, D. Price, W. Rack, G. H. Leonard, G. M. Brett, S. Urbini
Methodology: P. J. Langhorne, C. Haas, D. Price, W. Rack, G. H. Leonard, G. M. Brett

Fast Ice Thickness Distribution in the Western Ross Sea in Late Spring

P. J. Langhorne[1] , C. Haas[2] , D. Price[3] , W. Rack[3] , G. H. Leonard[4], G. M. Brett[3], and S. Urbini[5]

[1]Department of Physics, University of Otago, Dunedin, New Zealand, [2]Alfred Wegener Institute for Polar and Marine Research, Bremerhaven, Germany, [3]Gateway Antarctica, University of Canterbury, Christchurch, New Zealand, [4]School of Surveying, University of Otago, Dunedin, New Zealand, [5]Istituto Nazionale di Geofisica e Vulcanologia, Roma, Italy

Abstract We present a 700 km airborne electromagnetic survey of late-spring fast ice and sub-ice platelet layer (SIPL) thickness distributions from McMurdo Sound to Cape Adare, providing a first-time inventory of fast ice thickness close to its annual maximum. The overall mode of the consolidated ice (including snow) thickness was 1.9 m, less than its mean of 2.6 ± 1.0 m. Our survey was partitioned into level and rough ice, and SIPL thickness was estimated under level ice. Although level ice, with a mode of 2.0 m and mean of 2.0 ± 0.6 m, was prevalent, rough ice occupied 41% of the transect by length, 50% by volume, and had a mode of 3.3 m and mean of 3.2 ± 1.2 m. The thickest 10% of rough ice was almost 6 m on average, inclusive of a 2 km segment thicker than 8 m in Moubray Bay. The thickest ice occurred predominantly along the northwestern Ross Sea, due to compaction against the coast. The adjacent pack ice was thinner (by ~1 m) than the first-year fast ice. In Silverfish Bay, offshore Hells Gate Ice Shelf, New Harbor, and Granite Harbor, the SIPL transect volume was a significant fraction (0.30) of the consolidated ice volume. The thickest 10% of SIPLs averaged nearly 3 m thick, and near Hells Gate Ice Shelf the SIPL was almost 10 m thick, implying vigorous heat loss to the ocean (~90 W m^{-2}). We conclude that polynya-induced ice deformation and interaction with continental ice influence fast ice thickness in the western Ross Sea.

Plain Language Summary Sea ice held stationary by the coast is named fast ice. Around Antarctica, it is often observed near floating land ice and grounded icebergs. Fast ice is a critical habitat for marine life and known to be a sensitive indicator to changing weather and oceanic processes. Despite its importance, satellite measurements of its area are recent, and little is known about its thickness. Using a specialized instrument on a fixed wing aircraft, we measured the 2017 November fast ice thickness in the western Ross Sea. Most of the fast ice surveyed was 2 m thick on average and had formed in sheltered embayments. Where floating glaciers are in contact with fast ice, a 3–10 m thick layer of loose ice crystals was sometimes observed beneath, which contributed to its thickness. However, most of the thicker ice was rough ice, formed when ferocious offshore winds pushed ice from the coast. It then drifted with the prevailing ocean currents until eventually becoming frozen in place against coastal topography. This rough ice, 3.3 m thick on average and comprising half the surveyed volume, was significantly thicker than adjacent freely moving pack ice. Our survey provides a baseline from which future change can be measured.

1. Introduction

Antarctic land-fast sea ice (fast ice) is held stationary by the coastline, the seaward edge of floating ice tongues or shelves, or by icebergs grounded in the shallow waters of the continental shelf (Fraser et al., 2021; Giles et al., 2008). The seasonal loss of fast ice has been shown to affect the stability of ice shelves (Massom et al., 2018) and glacier tongues (Gomez-Fell et al., 2022; Stevens et al., 2013), hence also the Antarctic Ice Sheet coastal margins and outlet glaciers (Massom et al., 2001). Fast ice is of major ecological importance (Mezgec et al., 2017) as a breeding ground for species such as Weddell Seals (e.g., Ainley et al., 2015) and Emperor Penguins (e.g., Jenouvrier et al., 2021), as a nursery for fish species (Vacchi et al., 2012), and as a region of high primary productivity (Meiners et al., 2018). It is therefore imperative to understand the processes influencing fast ice formation and distribution, and drivers of temporal changes in the spatial coverage of fast ice.

Many factors are known to influence the distribution of fast ice (e.g., Fraser et al., 2021). There is mutual interaction with coastal polynyas that affects the rate of sea ice production through the rapid formation of frazil ice at the ocean surface (e.g., Nakata et al., 2021; Tamura et al., 2016), and plays a role in sculpting the fast ice/pack

ice edge (Nihashi & Ohshima, 2015). Their margins represent areas of dynamic ice deformation (Hollands & Dierking, 2016; Rack et al., 2021) and hence influence the development of the fast ice thickness distribution.

Marine-terminating continental ice also influences the coastal sea ice of Antarctica, with platelet ice contributing to the fast ice cover through ice-ocean interaction (Hoppmann et al., 2020; Langhorne et al., 2015). Melting at the base of ice shelves and outlet glaciers cools and freshens the ice shelf-ocean boundary layer, producing Ice Shelf Water (ISW) with a potential temperature below the surface freezing point (Foldvik & Kvinge, 1974; Jacobs et al., 1985). If the ISW moves to shallower depths, the rise in its pressure-dependent freezing point may force it to become supercooled in situ, causing frazil crystals to persist in the water column. These ice crystals may be deposited under ice shelves or ice tongues, and form marine ice (e.g., Frezzotti, 1997; Tison et al., 1998). The frazil ice can grow into larger platelet ice crystals which add to the mass of the coastal sea ice cover (e.g., Gough et al., 2012; Gow et al., 1998; Jeffries et al., 1993). Under conditions outlined by Wongpan et al. (2021) the crystals form a porous, friable layer, called the sub-ice platelet layer (SIPL) (Moreçki, 1965). The SIPL can be several meters thick (e.g., Arndt et al., 2020; Hughes et al., 2014), with ground-based, single-frequency and multifrequency electromagnetic induction measurements being used to map SIPL thickness, using numerical inversion methods (Brett et al., 2020; Hunkeler et al., 2015). Consequently, platelet ice formation not only causes sea ice to be thicker, but it also alters the hydrostatic relationship between sea ice freeboard and thickness, influencing satellite altimeter determination of sea ice thickness (Arndt et al., 2020; Brett et al., 2021; Price et al., 2014; Rack et al., 2013). Further, the stabilization of the upper water column by basal ice shelf melt, or by an influx of surface ice shelf meltwater (Bell et al., 2017), results in sea ice that is modeled to be ~0.2 m thicker than in a well-mixed scenario (Hellmer, 2004; Kusahara & Hasumi, 2014).

Progress has been made observing and understanding the factors controlling fast ice extent (Fraser et al., 2020, 2021), but fast ice thickness remains a particular challenge. While there are a few Antarctic embayments where the fast ice thickness distribution is well studied (e.g., Arndt et al., 2020; Brett et al., 2020), Giles et al. (2008) have carried out a more extensive study in East Antarctica using calibrated radar backscatter imaging to segregate fast ice into "smooth" and "rough" categories. They used proxy thicknesses of 1.7 m for "smooth" ice, and 5 m for "rough ice," based on observations of multiyear fast ice near a glacier (Massom et al., 2001). Giles et al. (2008) indicate that 33% of the fast ice is rough. Further they estimate that, although fast ice forms ~8% of the total November sea ice (fast and pack ice) area for the studied sector of East Antarctica in 1997 and 1999, it may comprise almost 30% of the total sea ice volume. Clearly the proportion of deformed ice in the fast ice cover is critical to an understanding of the overall fast ice thickness distribution.

Wide discrepancies still exist between Antarctic sea ice thickness estimates from satellite altimetry, largely due to the diversity of approaches to uncertainties in snow depth, and to the factors affecting the relationship between freeboard and ice thickness (e.g., Kacimi & Kwok, 2020; Price et al., 2019; Tian et al., 2021). These problems are exacerbated for fast ice. At present, hemispheric-scale satellite investigations of fast ice thickness do not exist, because proximity to the coast presents challenges and the lack of open water makes it very difficult to identify sea level (Brett et al., 2021; Price et al., 2013, 2015). Thus, the extensively studied, large fast ice zone of McMurdo Sound is an excellent site for trialing techniques. Price et al. (2013) used tide models in the derivation of satellite (ICESat) laser altimeter freeboards from 2003 to 2009, and found freeboard was strongly linked to the development and incorporation of an SIPL. Radar altimeter (CryoSat-2) also detects annual fast ice freeboard trends in line with known sea ice growth rates in McMurdo Sound (Price et al., 2015), while altimeter-derived thickness overestimates drill hole thickness because of buoyant forcing where there was a thick SIPL (Brett et al., 2021). The present study is motivated by the need for large-scale regional airborne measurements of fast ice thickness for comparison with satellite observations, and to better understand the coastal processes controlling fast ice distribution, including the partitioning into rough, dynamic and level, thermodynamic growth.

In this study, we use ice thickness data from airborne electromagnetic induction (AEM) sounding (Haas et al., 2010) to study the fast ice thickness distribution in the western Ross Sea within 30 days of its annual maximum extent (Fraser et al., 2021). Previous studies have analyzed AEM ice thickness surveys of pack ice in the western Ross Sea (Rack et al., 2021) and of fast ice and SIPL within the confines of McMurdo Sound (Haas et al., 2021; Rack et al., 2013). This is a first-time inventory of Antarctic fast ice thickness which can be used as baseline for future studies and to better understand processes of fast ice formation, thickness, and roughness. The particular questions being addressed are (a) what is the thickness distribution of fast ice along the Victoria Land coast; (b) what is the contribution of deformation to the fast ice thickness and volume distributions; and (c) where does a sub-ice platelet layer exist beneath the fast ice, and what is its contribution to volume?

2. The Icescape of the Victoria Land Coast

The coastal sea ice of Victoria Land between the McMurdo Ice Shelf and Cape Adare abuts 28 floating glaciers, ice tongues or ice shelves (Frezzotti, 1997), as indicated in Figures 1 and 2. The Hells Gate and McMurdo Ice Shelves display substantial areas of marine ice accreted at their base (Hoppmann et al., 2020; Tison et al., 1998), that sometimes reach the surface due to wind-induced ablation (Frezzotti, 1997). The floating glaciers south of Terra Nova Bay calve every few decades (Frezzotti, 1997) and are influenced by the presence or absence of fast ice (e.g., Gomez-Fell et al., 2022; Han & Lee, 2018; Stevens et al., 2013). Some are toughened against storms and wave action by marine ice at their base and within crevasses (Massom et al., 2018). Thus, interaction between continental ice and fast ice is a common feature of the Victoria Land coast, and we expect frazil/platelet ice and an SIPL to be present in some fast ice regions.

The western Ross Sea is also notable for polynya activity, with fast ice persistence, ice transport, and ISW formation driven by the complex interaction among three significant polynyas: the Ross Sea polynya (in front of the Ross Ice Shelf), the Terra Nova Bay polynya, and the McMurdo Sound polynya (e.g., Rack et al., 2021; Tison et al., 2020). The Ross Sea Polynya produces High Salinity Shelf Water (HSSW), generating ISW formation which flows into McMurdo Sound, and then northwards in a coherent coastal current that is conjectured to flow along the Victoria Land coast (Jendersie et al., 2018; Stevens et al., 2017). HSSW is also generated by opening events of the Terra Nova Bay Polynya (e.g., Fusco et al., 2009; Yoon et al., 2020), influencing fast ice persistence and ice transport along the coast. The McMurdo Sound Polynya influences the fast ice edge in McMurdo Sound (e.g., Leonard et al., 2021).

The thickness distribution of an SIPL is largely conditioned by ocean heat flux (e.g., Langhorne et al., 2015; Lewis & Perkin, 1985; McPhee et al., 2016; Wongpan et al., 2021). Evidence for the cold, coherent, northward-moving current (Stevens et al., 2017) links our study area to the extensively studied ISW plume of McMurdo Sound (e.g., Barry, 1988; Lewis & Perkin, 1985; Mahoney et al., 2011; Robinson et al., 2014), with its resulting SIPL thickness distribution (e.g., Gow et al., 1998; Haas et al., 2021; Hughes et al., 2014; Price et al., 2014). These studies showed that an SIPL occurs in a 20–30 km wide, 40–80 km long region extending from the northern tip of the McMurdo Ice Shelf in a north-westerly direction. At the end of winter the thickness of the SIPL under first-year ice can be up to 7.5 m (Hughes et al., 2014; Price et al., 2014), coinciding with more than 2.5 m of consolidated sea ice. The distribution of the SIPL in McMurdo Sound is remarkably consistent from year to year under fast ice (Langhorne et al., 2015), with interannual variability related to polynya activity (Brett et al., 2020).

Terra Nova Bay is bordered to the south by the Drygalski Ice Tongue, and to the north by the Campbell Ice Tongue (which is situated between Gerlache Inlet and Silverfish Bay in Figure 2; see also Figure 7). The Drygalski Ice Tongue acts as a barrier for pack ice advection from the south and the south-west, while katabatic winds blow offshore and sporadically keep the Terra Nova Bay polynya area ice free (e.g., Fusco et al., 2009). The Drygalski Ice Tongue is also a barrier to the proposed northward-flowing cold current (Stevens et al., 2017). In Terra Nova Bay itself marine ice and ISW are common features (e.g., Budillon & Spezie, 2000; Frezzotti, 1997; Tison et al., 1998; Yoon et al., 2020). A wind-driven cyclonic gyre dominates the upper ocean of Terra Nova Bay (Van Woert et al., 2001), directing surface currents mainly north-east along the coast (Budillon & Spezie, 2000). Close to the coast, Terra Nova Bay Ice Shelf Water (TISW) arises due to the interaction of the shallow-intermediate layers of HSSW with the coastal glaciers (Budillon & Spezie, 2000). In addition, TISW near the Nansen Ice Shelf is advected northwards with the cyclonic circulation (Yoon et al., 2020). The fast ice of the region is strongly affected by ISW, forming platelet ice (Vacchi et al., 2012).

The Hells Gate Ice Shelf is a small ice shelf separated from the Nansen Ice Shelf by Inexpressible Island (Figure 2). It is composed almost entirely of marine ice (Souchez et al., 1991; Tison et al., 1998) due to high surface ablation combined with basal accretion of sea water. It is well known that the sea ice in front of the Hells Gate Ice Shelf is heavily influenced by locally and regionally generated ISW (Tison et al., 1998).

In the northern part of our study area (see Figures 1 and 2) there is less information on the fast ice and the extensiveness of its interaction with marine-terminating ice bodies. Moubray Bay is a location of almost year-round fast ice in the western Ross Sea (Ainley et al., 2015), and the timing of freeze-up and breakup during the 21st century does not differ significantly from that in the 1960s in Moubray Bay (Ainley et al., 2015; Fraser et al., 2020).
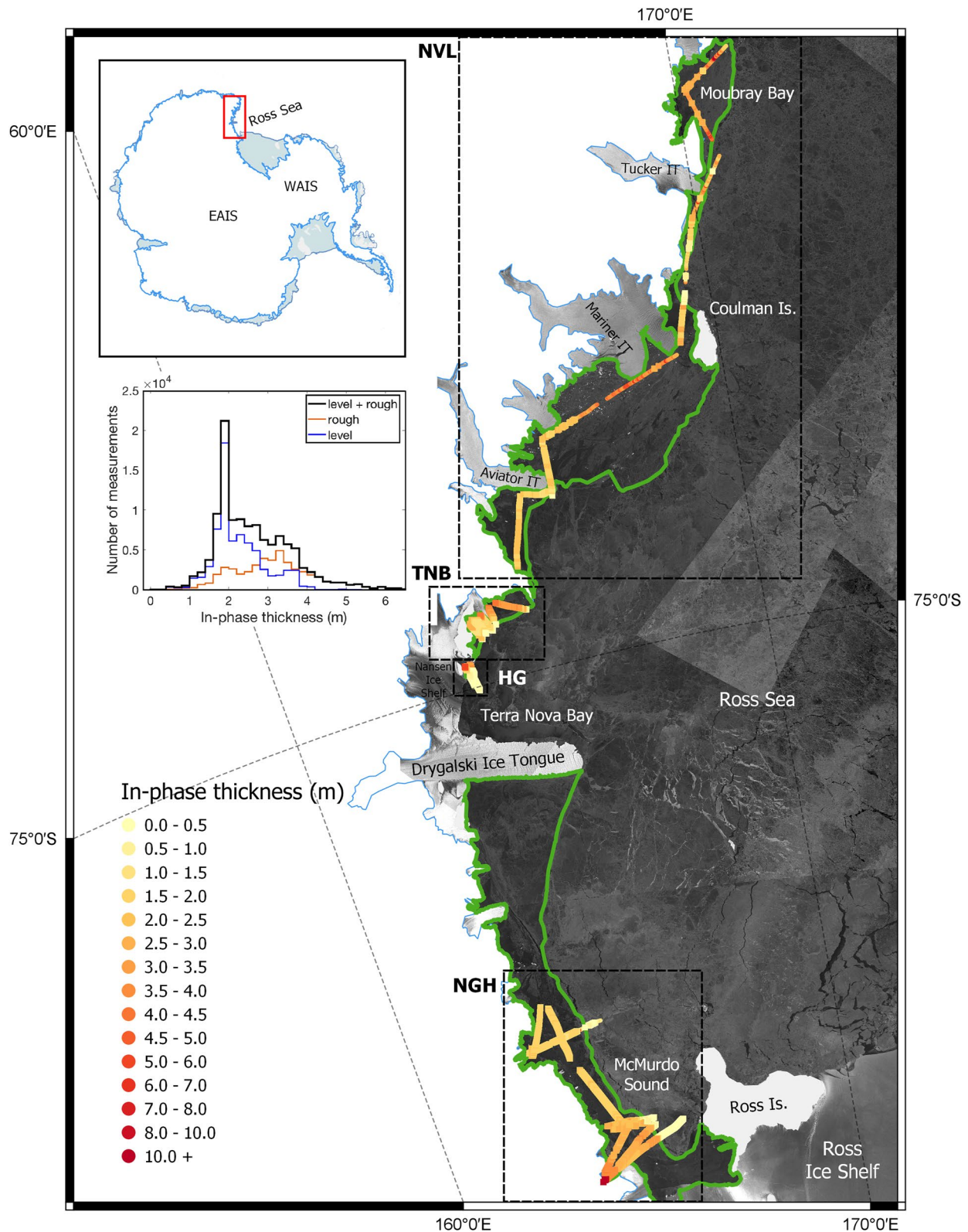
Figure 1. In-phase apparent thickness (h_I), smoothed with 100-point median filter, for entire coastal survey displayed on Sentinel-1 Interferometric Wide (IW) swath mode image mosaic; images acquired between 10 and 20 November 2017. Level ice thickness is thicker line (squares), rough ice is thinner line (circles). Boxes show bounds of Figure 5 (New Harbor and Granite Harbor, NGH), Figure 6 (Hells Gate Ice Shelf, HG), Figure 7 (Terra Nova Bay, TNB), Figure 8 (North Victoria Land Coast, NVL). Survey located on Antarctic overview map (top left). Fast ice edge indicated by green line. Histogram insert shows distribution of the level, rough and all in-phase apparent thicknesses of fast ice within the green ice edge.
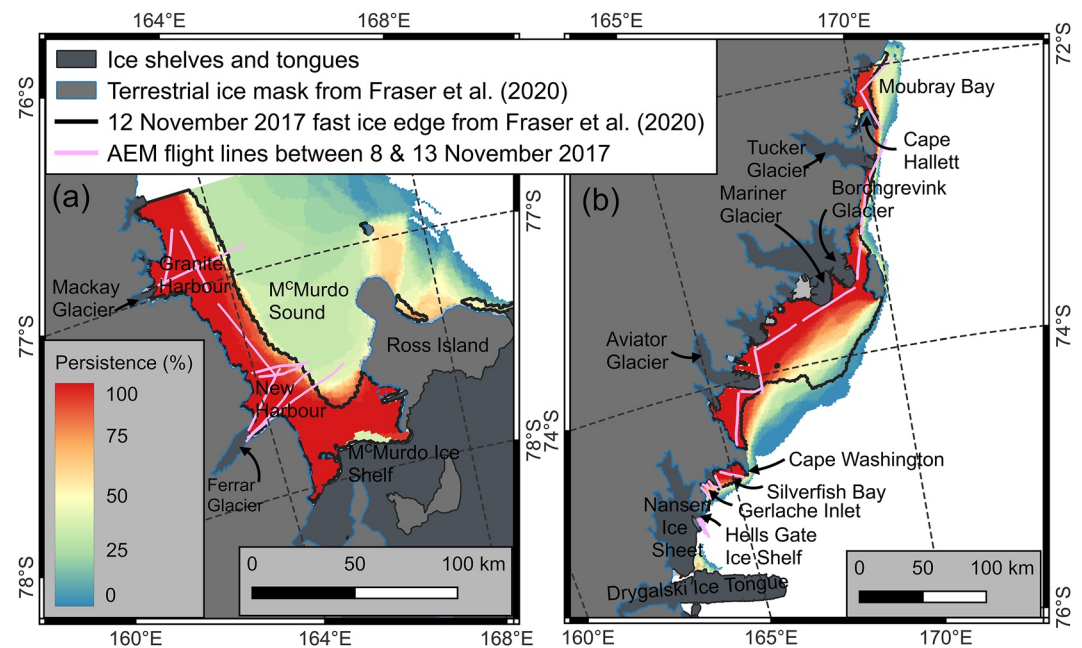
Figure 2. Map of coastline of (a) McMurdo Sound to Granite Harbor and (b) Victoria Land north of 75°S (cf. Figure 1). Fast ice persistence in November taken from Fraser et al. (2020) data set for 2000–2018. Ice shelves and tongues shown in dark gray. Light gray pixels are the terrestrial ice mask from Fraser et al. (2020). Fast ice edge determined by Fraser et al. (2020) for 12 November 2017 indicated by black line. Airborne electromagnetic induction (AEM) flight lines between 8 and 13 November 2017 shown in magenta.

3. Methods

3.1. Instrumentation and Area of Investigation

The AEM survey flights took place on 8, 9, 10, and 13 November 2017, with coastal flight tracks shown in Figures 1 and 2. The study area extended 700 km along the Victoria Land coast of the western Ross Sea from New Harbor (77.7°S, 164.0°E) to near the Adare Peninsula (72.0°S, 171.5°E). Dates of acquisition of all data presented are given in Table S1 in Supporting Information S1.

The AEM surveys were carried out with an EM sensor ("EM Bird") towed beneath a Basler BT67 aircraft, a turbo DC3. The EM Bird was flown with an average speed of 120 knots at mean heights of 16 m above the ice surface (Haas et al., 2010). It was operated in vertical dipole mode with a signal frequency of 4,060 Hz and a spacing of 2.67 m between transmitting and receiving coils (Haas et al., 2009). The sampling frequency was 10 Hz, corresponding to a sample spacing of approximately 6 m. A Riegl LD90 laser altimeter was used to measure the Bird's height above the snow/ice surface, with a range accuracy of ±0.025 m (Haas et al., 2021). At this height the footprint of the AEM measurements is about 45 m. Georeferenced photographs were taken of the snow/ice surface from an altitude of 100 m with an aircraft-mounted Canon EOS 5D Mark III nadir-looking camera with a 24 mm lens.

The single-frequency AEM measurements record in-phase and quadrature signals representing the amplitude and phase of the induced secondary field relative to the primary field transmitted by the EM Bird. Over level ice and in the absence of an SIPL, total (snow plus ice) thicknesses determined from in-phase and quadrature measurements agree within an accuracy of ±0.10 m (Haas, 2004, 2006; Haas et al., 2009; Pfaffling et al., 2007). In rougher ice the maximum thickness of pressure ridges or rubble fields is generally underestimated due to their three-dimensional shape and porosity, resulting in up to 50% underestimation of the "true" thickness of unconsolidated ridges (e.g., Haas & Jochmann, 2003; Pfaffling et al., 2007). As we do not know the snow thickness, we assume that it is similar throughout the study region and less than 10% of the total ice thickness (Fons & Kurtz, 2019; Tison et al., 2020). In what follows, we treat level ice as a 3-layer system (snow + consolidated ice, the sub-ice platelet layer (SIPL) and sea water) and retrieve the thickness of the SIPL in addition to that of snow + ice (e.g., Haas et al., 2021; Rossiter & Holladay, 1994).

3.2. Identifying the Sub-Ice Platelet Layer

From multiple years of AEM measurements over level fast ice in McMurdo Sound, a method has been developed to find the thickness of the high porosity/higher conductivity sub-ice platelet layer, h_{sipl}, at the base of the sea ice (Haas et al., 2021). Beneath level ice, the porous SIPL causes a deviation of the in-phase- and quadrature-derived retrievals. In that case, we call the AEM-derived thicknesses *apparent thickness*, as they differ from the "true" thickness of fully consolidated ice of negligible conductivity (Haas et al., 2021). In the presence of an SIPL, the in-phase-derived apparent thickness (from now on termed in-phase apparent thickness) is greater than the true consolidated ice thickness, but less than the thickness of the consolidated ice plus SIPL (Haas et al., 2009; Rack et al., 2013). On the other hand, the apparent quadrature-derived thickness (from now on called quadrature apparent thickness) is less affected by the presence of an SIPL (Haas et al., 2021) and is close to the "true" thickness. Thus, the thickness of the SIPL can be derived from the difference between the apparent in-phase and quadrature thicknesses.

However, due to the low signal-to-noise ratio of the quadrature signals, SIPL data are very noisy and smoothing is necessary. Over level fast ice typical SIPL thickness variations are sufficiently gradual that smoothing does not remove information. Therefore, unless stated otherwise, here we first smoothed apparent in-phase and quadrature thickness data with a 100-point median filter; that is, smoothed over approximately 600 m. Then, following Haas et al. (2021), h_{sipl} is found using

$$h_{sipl} \approx (h_I - h_Q) / \alpha$$

where h_I and h_Q are the apparent thickness of the in-phase and quadrature measurements, respectively, and the SIPL scaling factor, $\alpha = 0.4$, was determined by calibrating against drill hole thickness measurements in McMurdo Sound in November 2017 (Haas et al., 2021). The uncertainty in SIPL thickness of ± 0.5 m is greater than that of typically ± 0.1 m in consolidated ice thickness (Haas et al., 2021). The noise in the quadrature signal can cause it to be larger than the in-phase value, resulting in the possibility of negative values of SIPL with magnitudes up to ~ 0.5 m.

In extensive deformed ice and rubble fields, the blockiness of the ice keels also results in porous layers which affect the EM signal in a similar way to the SIPL, again causing the in-phase-derived and quadrature-derived apparent sea ice thicknesses to deviate (Figure 3). Consequently, the SIPL cannot be found unambiguously under rough ice. We overcome this additional challenge by distinguishing level from rough ice, and calculating SIPL thickness only under level ice.

3.3. Discriminating Level Ice From Rough Ice

Numerous methods have been used to distinguish level ice from deformed, rough ice (e.g., Beckers et al., 2015; Giles et al., 2008; Rabenstein et al., 2010; Tin & Jeffries, 2001; Von Albedyll et al., 2021; Wadhams & Horne, 1980). Here we identified sections of level ice from rough ice by modifying the method of Rabenstein et al. (2010) and Von Albedyll et al. (2021). We find the absolute value of the point-by-point, unsmoothed, vertical, in-phase thickness gradient, $\Delta h_I / \Delta x$, and smooth it over 101 points (approximately 600 m of profile length) using a centered moving median filter. Level ice is defined where the filtered gradient is smaller than 0.006, a value chosen by Von Albedyll et al. (2021). Allowing for small variations in flight speed, we conservatively take the minimum possible separation between along-profile samples, Δx, as 5 m, while Δh_I is the difference in unsmoothed, in-phase apparent thickness between adjacent EM measurements. Thus, ice is categorized as level at position n if

$$\widehat{\Delta h_I(n)} = \text{median}\{\Delta h_I(n - M), ..., \Delta h_I(n + M)\} < (0.006 \times 5\,\text{m}) = 0.03\,\text{m}$$

where $M = 50$. Rough ice is defined where

$$\widehat{\Delta h_I(n)} \geqslant 0.03\,\text{m}$$

Assuming that the AEM sample points, Δx, are equidistant and that the width of the AEM footprint does not change during the survey, the fraction of transect length, L, and fraction of transect volume, V, that are level or rough are, respectively, defined as
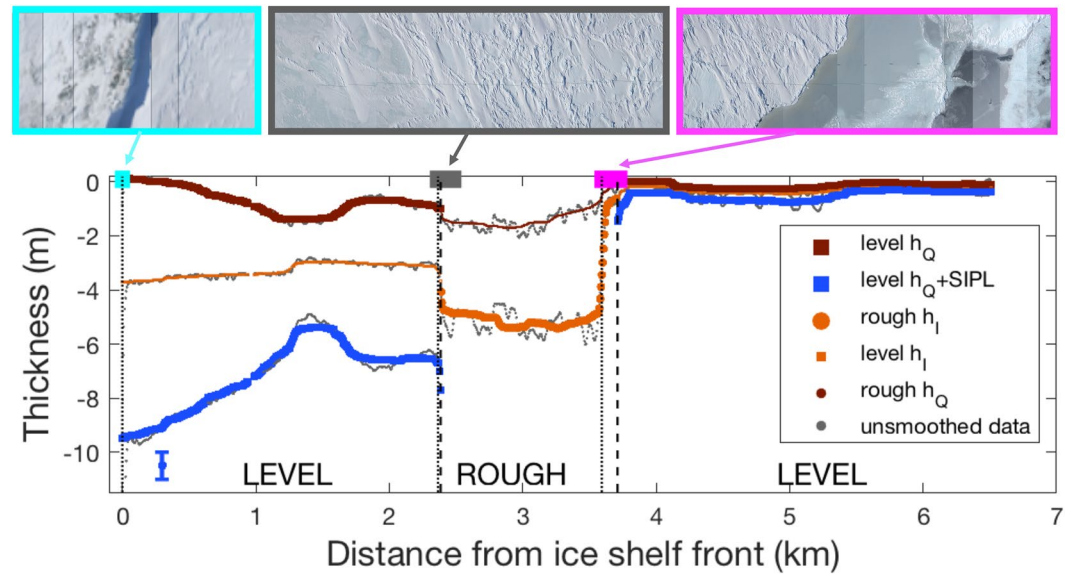
Figure 3. Illustration of the identification of rough and level ice and the sub-ice platelet layer (SIPL) off the Hells Gate Ice Shelf (Ice Shelf shown in left of photo mosaic). Thicknesses are shown downwards from snow/ice surface at 0 m, plotted against distance from ice shelf front. In-phase and quadrature apparent thicknesses under rough (circles) and level (squares) fast ice are compared. Unsmoothed data in gray. All other data are smoothed with 100-point median filter. Quadrature apparent thickness (h_Q) in brown, quadrature plus SIPL in blue (uncertainty indicated by bar), and in-phase apparent thickness (h_I) in orange. Under level ice h_Q represents the consolidated ice thickness, while for rough ice h_I is the best measure, as denoted by larger symbols. Photo mosaics of sea ice surface features, showing transitions from ice shelf to nearshore level ice (cyan), from nearshore level to rough ice (gray), and from rough to pack ice (magenta). Boundaries identified from aerial photographs (dotted) and roughness algorithm (dashed) shown as vertical lines.

$$L = \frac{N_k}{N} \text{ and } V = \frac{\sum_{k=1}^{N_k} h_k}{\sum_{i=1}^{N} h_i}$$

where N is the total number of samples in the transect, N_k the number of thickness samples from either level or rough ice, and h is the respective thickness (Rack et al., 2021).

Aerial photographs were taken from the aircraft at an altitude of approximately 100 m above the ice to verify the robustness of the rough ice detection algorithm. Figure 3 demonstrates the verification of transitions between ice types just offshore from the Hells Gate Ice Shelf. The maximum lateral difference between the transition identified by the algorithm, and that identified visually from aerial photographs, is in the order of 200 m, and generally less than 50 m. Figure 3 also illustrates that in this section of the survey the in-phase and quadrature apparent thicknesses differ by several meters over both rough and level ice. As discussed above, this difference results from a porous layer under the ice, but we are unable to distinguish between blocks of ice in rubble keels and an SIPL. Consequently, in this paper we take the conservative approach of reporting only in-phase apparent thickness under rough ice, that is, we do not attempt to infer the presence and thickness of an SIPL. In contrast, under level ice the quadrature apparent thickness represents the consolidated snow + ice thickness and an SIPL can be calculated with an uncertainty of ±0.5 m (Haas et al., 2021). Our chosen measures over level and rough ice are denoted by larger symbols in Figure 3 (appearing as thicker lines).

3.4. Delineating the Boundary Between Fast Ice and Pack Ice

In November 2017, the area covered by land-fast sea ice in the Ross Sea was 2% of the total sea ice area (Li et al., 2020), typical of the eight Novembers examined in the Li et al. study. Fraser et al. (2020, 2021) have recently produced a continuous, high spatio-temporal resolution (1 km, 15 days) time series of circum-Antarctic fast ice extent from March 2000 to March 2018 (see Figure 2 and Figure S1 in Supporting Information S1 for this data set in the western Ross Sea). Figure 2 shows the likelihood of finding fast ice in a pixel during the month of November over the years 2000–2018 (Fraser et al., 2020), with flight tracks from the present survey

Table 1
Statistics of Fast Ice Thickness in Western Ross Sea, cf. Figure 4a

Section	Number of meas.	$h_{mean} \pm$ standard deviation (m)	h_{mode} (m)	h_{median} (m)	h_{max} (m)	h_{H10} (m)	L (%)	V (%)
ALL								
Fast ice traversed (h_I)	115,080	2.63 ± 1.03	1.87	2.42	11.40	4.78		
Rough (h_I)	46,625	3.22 ± 1.19	3.31	3.15	11.40	5.66	41	50
Level consolidated (h_Q)	68,383[a]	2.01 ± 0.58	1.97	1.95	4.40	3.11	59	50
Level SIPL	68,383[a]	0.56 ± 1.01	0.05	0.37	9.64	2.67		
SOUTH of 75°S								
Fast ice traversed (h_I)	51,210	2.43 ± 0.76	1.87	2.31	6.65	3.95		
Rough (h_I)	9911	3.05 ± 0.96	2.93	3.04	6.65	4.92	19	24
Level consolidated (h_Q)	41,265[a]	2.03 ± 0.54	1.97	1.98	3.79	3.12	81	76
Level SIPL	41,265[a]	0.61 ± 0.91	0.35	0.41	5.64	2.48		
NORTH of 75°S								
Fast ice traversed (h_I)	63,870	2.80 ± 1.18	1.91	2.56	11.40	5.24		
Rough (h_I)	36,714	3.27 ± 1.25	3.31	3.18	11.40	5.80	58	67
Level consolidated (h_Q)	27,118[a]	1.97 ± 0.62	1.87	1.89	4.40	3.10	42	33
Level SIPL	27,118[a]	0.49 ± 1.15	0.02	0.18	9.64	2.84		

Note. h_{H10} is the mean of the thickest 10% of ice thicknesses. L and V are the fraction of transect length and volume, respectively.

[a]h_Q is not determined in less than 0.07% cases where h_I is found.

superimposed. In this paper, Fraser et al. (2020) is the primary guide to identify the fast ice edge. Then, as a secondary guide, we use Sentinel-1 and MODIS imagery on the days of the AEM surveys to delineate fast ice from pack ice at a more suitable resolution for the EM thickness surveys. We also ensure that all ice present in the fast ice data set has persisted for at least 15 days, and is mechanically fastened to shoreline features.

4. Results

4.1. Fast Ice Statistics of Western Ross Sea

The fast ice extent in November 2017 (see Figure 2) was typical of November 2000-2018 (Fraser et al., 2020), as illustrated in Figure S1 in Supporting Information S1. An examination of MODIS visual imagery from October 2016 to April 2017 implies that most of the surveyed fast ice was first-year ice, with open water observed at some time during summer along most of the AEM survey lines. Only within 9 km of the front of the Ferrar Glacier in New Harbor (see Figures 1 and 2) did the fast ice remain in place through the summer of 2016/2017. Rack et al. (2021) have provided a description of events immediately preceding the observed coastal and fast ice thickness distributions of November 2017. In the absence of strong wind events, pack ice in the area generally drifts northwards. A strong polynya event on 4 October 2017 pushed ice toward the northwest from the Ross Sea and McMurdo Polynyas toward the Drygalski Ice Tongue, and toward Terra Nova Bay (left panel of Figure 1 in Rack et al.). After this event, the ice drifted to the northeast again (right panel of Figure 1 in Rack et al.). Events like this created the rough ice in front of Hells Gate Ice Shelf, and on the margins of the fast ice of Silverfish Bay (see Figures 1 and 2). Multiple such events occur every year (Tison et al., 2020), sculpting the fast ice edge.

Figure 1 shows the in-phase apparent thickness of all the coastal sea ice surveyed (including minor fractions of pack ice immediately adjacent to the fast ice edge) in November 2017. In addition, the in-phase thicknesses are separated into level and rough ice, using the algorithm described in Section 3.3. Of more than 800 km of coastal sea ice (fast and pack) surveyed, approximately 700 km was over fast ice, of which 59% by transect length (50% by transect volume) was level ice (see Table 1). In this paper, we focus on the ice within the fast ice boundary defined as described in Section 3.4, which removes ice less than 0.1 m thick indicative of new ice or open water in polynyas and leads adjacent to the fast ice edge (see insert of Figure 1).

Table 1 and Figure 4 report statistics for two regions of similar number of data points. "South of 75°S," includes New Harbor and Granite Harbor (NGH box in Figure 1) but excludes any McMurdo Sound data reported
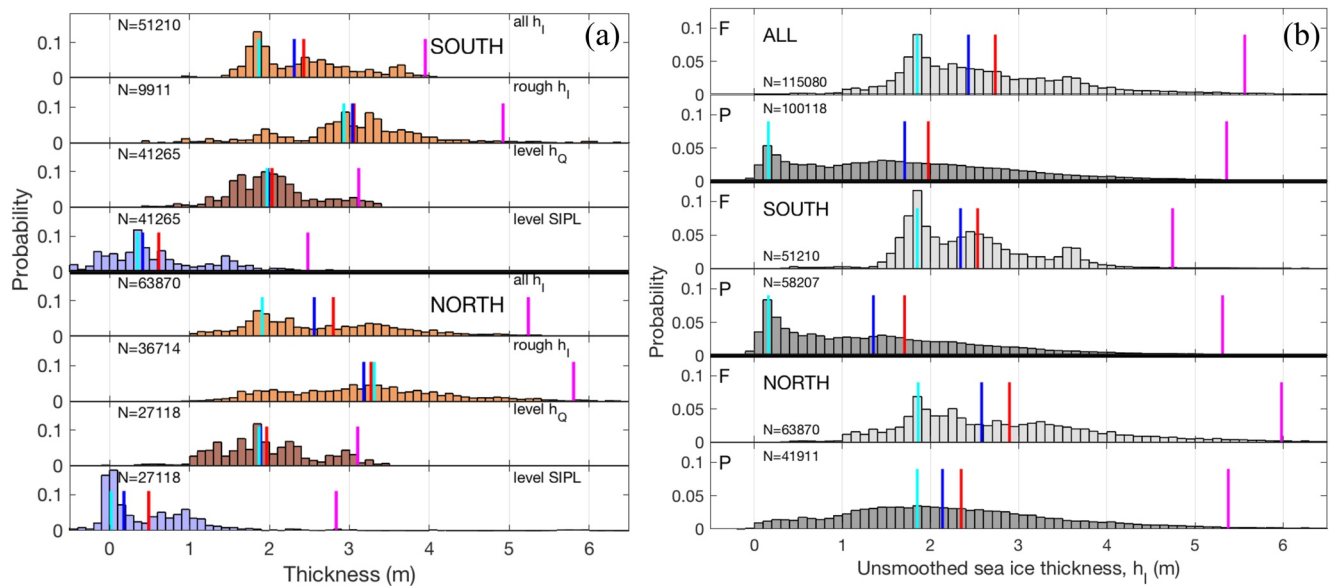
Figure 4. (a) Probability distributions of 100-point median filtered fast ice thicknesses in western Ross Sea in November 2017. Upper four panels show "south of 75°S," lower four panels "north of 75°S." Panels show all in-phase apparent thicknesses h_I in orange, rough h_I in orange, level h_Q in brown, and SIPL in blue. The mean (red), median (blue), mode (cyan), and h_{H10} (magenta) bars are shown for each distribution. The number of samples (N) in each data set is given. (b) Probability distributions of unsmoothed in-phase apparent thicknesses (h_I) in the western Ross Sea in November 2017, comparing fast ice with pack ice from Rack et al. (2021). Top two panels compare all fast ice (F) with all pack ice (P) thicknesses. Fast ice (F) and pack ice (P) data "south of 75°S" and "north of 75°S" are compared in the middle and bottom two panels, respectively. The mean (red), median (blue), mode (cyan), and h_{H10} (magenta) bars are shown for each distribution. The number of samples (N) in each dataset is given.

elsewhere (Haas et al., 2021). "North of 75°S" includes the sea ice in front of the Hells Gate Ice Shelf (HG box in Figure 1); the Gerlache Inlet/Silverfish Bay region of Terra Nova Bay (TNB box in Figure 1), in addition to a 400 km transect up the coastline of northern Victoria Land from Cape Washington to Cape Adare (box NVL in Figure 1).

The modal thickness of all level fast ice surveyed was 2.0 m (mean = 2.0 ± 0.6 m) (see Table 1 and Figure 4), consistent with first-year thermodynamic fast ice formation in the area (e.g., Leonard et al., 2006). Noting the uncertainty of ±0.5 m in SIPL thickness determination, under level ice an SIPL was found in some areas with an overall mean of 0.6 ± 1.0 m and mode = 0.1 m (see Table 1 and Figure 4a). This disguises the fact that in some locations the SIPL may be up to almost 10 m thick, and the thickest 10% has an average thickness of 2.7 m (Table 1). The modal thickness of the rough ice was 3.3 m (mean = 3.2 ± 1.2 m, Table 1 and Figure 4a), with a maximum fast ice thickness of over 11 m in Moubray Bay at the northern end of the survey (Table 1).

As anticipated the mode of the thermodynamically grown, level fast ice in the north is thinner than in the south, but only by 0.1 m (1.9 m cf. 2.0 m in Table 1 and Figure 4a). However overall the northern ice has a mean that is 0.4 m thicker (2.8 m cf. 2.4 m in Table 1 and Figure 4a) because of the higher proportion of rough, deformed ice in the north (58% cf. 19% by length in Table 1).

In Table 2, we compare our fast ice data with the pack ice thickness offshore, surveyed at the same time and reported in Rack et al. (2021). In this case, unsmoothed, in-phase apparent thickness data are used for pack and fast ice as these are appropriate for pack ice data. The mean and median of our 700 km survey of fast ice thicknesses are approximately 0.7 m (~30%–40%) greater than the 800 km survey of pack ice in the same region (see Table 2 and Figure 4b), while the mode is more than 1.5 m greater in the fast ice. Thus, while the area covered by fast ice is small, its contribution to sea ice volume is significant.

4.2. Results and Discussion of Subregions

In the following, we split the survey into segments, moving south to north. There are four embayments: New Harbor and Granite Harbor (NGH box in Figure 1); in front of the Hells Gate Ice Shelf (HG box); the Gerlache

Table 2
Statistics of Pack Ice Thickness (Unsmoothed Data From Rack et al. (2021)) From Western Ross Sea, November 2017 Compared With Fast Ice Thickness (Unsmoothed From Present Work), cf. Figure 4b h_{H10} Is the Mean of the Thickest 10% of Ice Thicknesses

Section	Number of measures	$h_{mean} \pm$ standard deviation (m)	h_{mode} (m)	h_{median} (m)	h_{max} (m)	h_{H10} (m)
ALL						
Fast ice traversed (h_I)	115,080	2.73 ± 1.30	1.85	2.43	24.80	5.56
Pack ice traversed (h_I)	100,118	1.97 ± 1.56	0.16	1.71	15.58	5.36
SOUTH of 75°S						
Fast ice traversed (h_I)	51,210	2.53 ± 1.10	1.85	2.34	24.80	4.75
Pack ice traversed (h_I)	58,207	1.71 ± 1.59	0.16	1.35	11.78	5.31
NORTH of 75°S						
Fast ice traversed (h_I)	63,870	2.90 ± 1.43	1.86	2.58	19.60	5.98
Pack ice traversed (h_I)	41,911	2.35 ± 1.44	1.85	2.14	15.58	5.38

Inlet/Silverfish Bay region of Terra Nova Bay (TNB box), in addition to a 400 km transect up the coastline of northern Victoria Land from Cape Washington to Cape Adare (box NVL in Figure 1).

4.2.1. Granite Harbor and New Harbor (NGH)

While the sea ice in the area was mostly first-year ice, within 9 km of the front of the Ferrar Glacier in New Harbor there was ice that had persisted throughout the summer 2016/2017 (see Figure 5c), where the transition can be seen from second year ice of about 3.0 m thickness, to first-year ice of 2.1 m. The fast ice in this area was influenced by the grounded tabular iceberg shown in Figures 5a and 5b, which had been in this approximate position and orientation since March 2014. All fast ice in Granite Harbor had been in place for less than 8 months. Granite Harbor and New Harbor (Figures 5a and 5b) are regions where platelet ice has previously been reported as a casual reference to its presence within some other study (e.g., Barry, 1988; Cummings et al., 2019; SooHoo et al., 1987; Stockton, 1983).

Here level ice comprised 81% of the cover by length (see Figure 5 and Table 1, SOUTH). The modal thickness of the consolidated level ice was 2.0 m, consistent with thermodynamically grown first-year fast ice (e.g., Leonard et al., 2006); its mean was 2.0 ± 0.5 m. The mean SIPL thickness of 0.6 ± 0.9 m was considerably larger than the mode of 0.3 m, indicating a skewed distribution with a maximum of 5.6 m (Table 1, SOUTH). Figure 5b demonstrates that generally the SIPL was thicker close to the coast and toward the south. A possible source of ISW to maintain this SIPL distribution is the proposed coherent current that moves northwards from the McMurdo Ice Shelf to beyond Granite Harbor (Stevens et al., 2017).

However, local sources may also contribute to platelet ice formation. Five approximately east-west transects of Figures 5a and 5b have been plotted in Figure 5c. The decrease in SIPL is evident, from between 2 and 5 m thick at the coastal edge, to approximately zero at the outer fast ice edge. The exception is transect E-F where an SIPL approx. 1.5 m thick was observed along the entire length of the transect. This transect was closest to the location (at label "New Harbor" in Figure 5a) of previous observations of ice crystals beneath multiyear sea ice (Murray et al., 2013), and close to submarine ice cliffs at the mouth of the Taylor Valley (Murray et al., 2013; Stockton, 1983). This implication of supercooled water, along with the inferred existence of anchor ice at the head of the Ferrar Glacier (Mager et al., 2013), suggests that the glacier terminus of the Ferrar may be a local source of supercooled water providing km-scale spatial variations in SIPL thickness. In particular, the 3 m thick SIPL at location A (see Figures 5a and 5b) is 120 km distant from the McMurdo Ice Shelf as a potential source of ISW. The SIPL is more likely sourced beneath the floating tongue of the Mackay Glacier (Debenham, 1965; Frezzotti, 1997). Formation of an SIPL around a floating glacier tongue is not unprecedented, such observations having been reported around the Erebus (Stevens et al., 2014) and Drygalski (Stevens et al., 2017) ice tongues.

Alternatively, underwater ice crystal formation may be caused by the double diffusive effects of cold, saline brines entering the ocean through subsurface connections with inland lakes, aquifers, and subglacial waters (Foley et al., 2019). Such connections have been identified beneath the Ferrar Glacier, where subglacial brines have been shown to have an open connection directly into the Ross Sea, and at the submarine ice cliffs where Lake Fryxell in the lower Taylor Valley is connected to a deeper aquifer beneath the lake to the Ross Sea (Foley
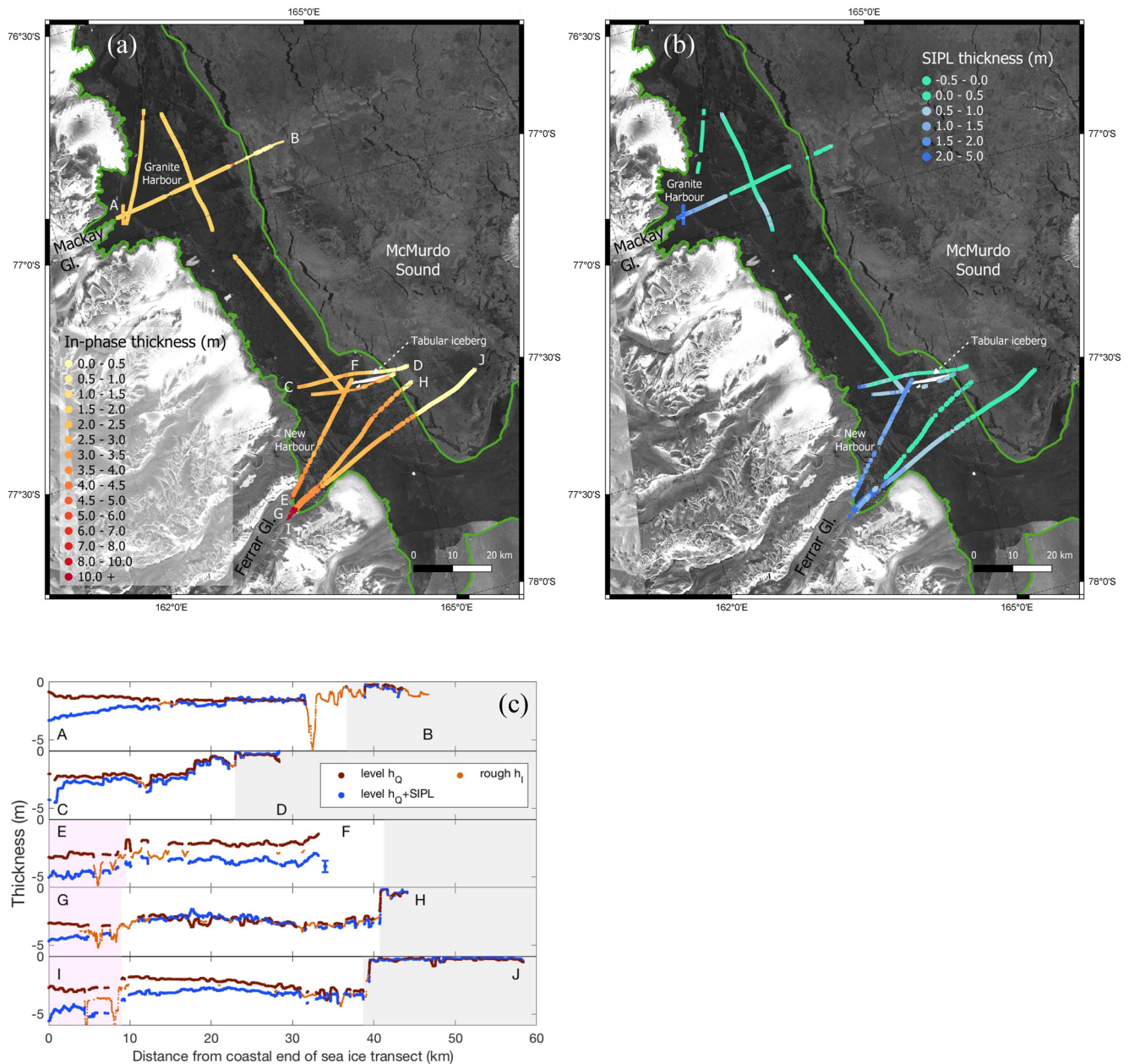
Figure 5. New Harbor and Granite Harbor. (a) In-phase apparent thickness (h_I) plotted on Sentinel-1 Interferometric Wide (IW) swath mode image acquired 14 November 2017 21:22 UTC. Locations A–J identified. Level ice shown as thicker line (squares), rough ice as thinner line (circles). Fast ice edge indicated by green line. (b) As (a) but for SIPL thickness under level ice. (c) Five transects bounded by locations A–J, plotted against distance from coastal end of transect. Thickness measured downwards from snow/ice surface at zero. Consolidated level ice thickness (h_Q) in brown, and consolidated ice thickness plus SIPL in blue (uncertainty indicated by bar in panel E–F). Rough ice thickness (h_I) in orange. Second year ice shaded pink, regions outside the fast ice edge shaded gray.

et al., 2019). Extreme halophiles have been observed in New Harbor, supporting the hypothesis of this submarine discharge (Currie et al., 2021).

4.2.2. Sea Ice in Front of Hells Gate Ice Shelf (HG)

In the vicinity of the Hells Gate Ice Shelf, three distinct regions are identified on radar images, aerial photos, and ice thickness data (Figures 3 and 6). The SAR images of Figures 6a and 6b show level sea ice close to the ice shelf, bounded to the south by a triangular-shaped region of rough ice (Zhai et al., 2019). This ice was first-year ice, much of which became established around 25 September (from time series of MODIS images and Zhai et al., 2019), just prior to the deformation event discussed above. The exceptions were first-year ice shoreward
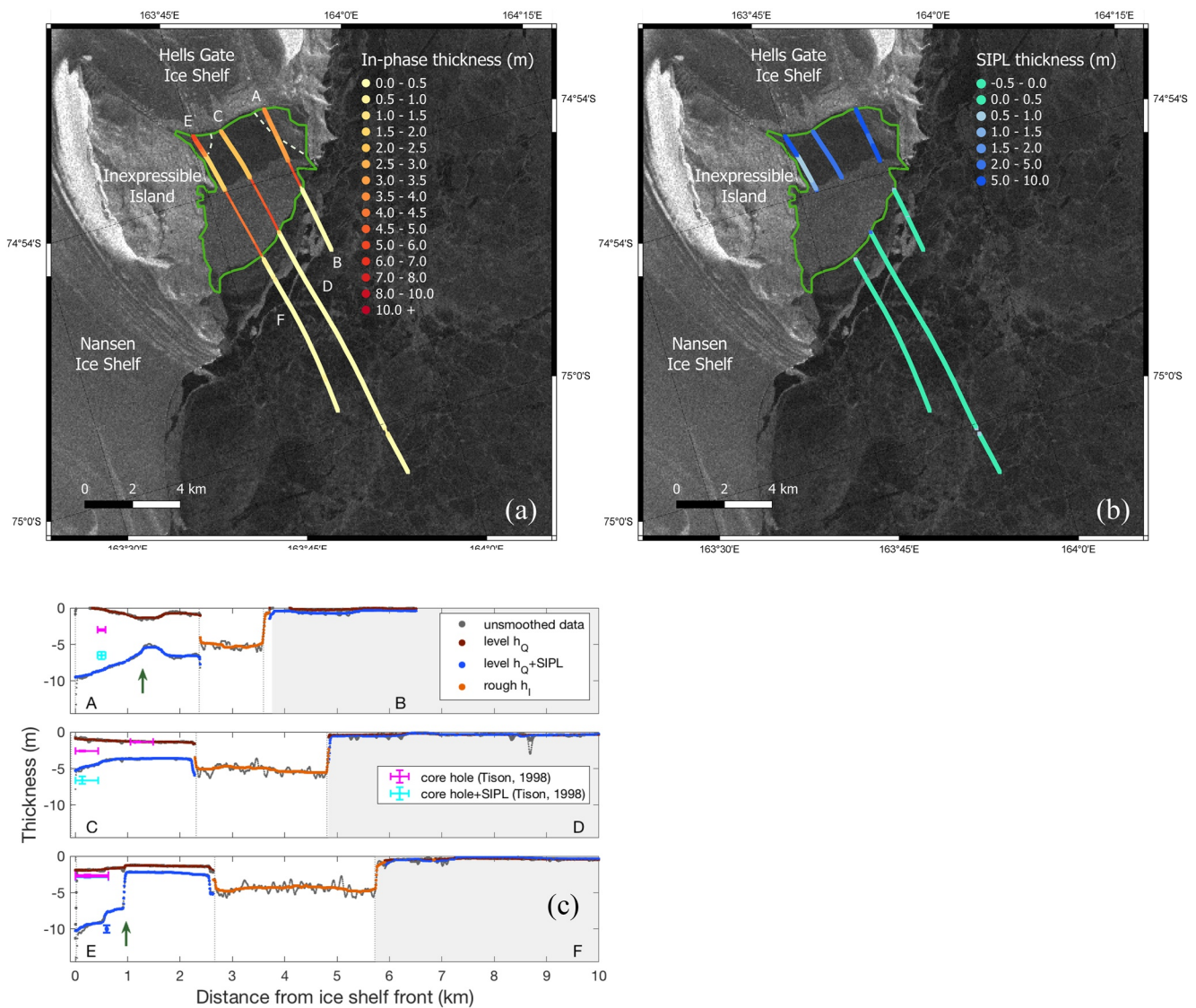
Figure 6. Sea ice in front of Hells Gate Ice Shelf (a) In-phase apparent thickness (h_I) plotted on Sentinel-1 Interferometric Wide (IW) swath mode image acquired 10 November 2017 10:29 UTC. Locations A–F identified. Level ice shown as thicker line (squares), rough ice as thinner line (circles). Fast ice edge indicated by green line. Ice older than 45 days is coastward of dashed pale green line. (b) As (a) but for SIPL thickness under level ice. (c) Three transects, bounded by locations A–F, plotted against distance from ice shelf front. Thickness measured downwards from snow/ice surface at zero. Unsmoothed data shown in gray. All other data smoothed with 100-point median filter. Consolidated level ice thickness (h_Q) in brown, and consolidated ice thickness plus SIPL in blue (uncertainty indicated by bar in panels E–F). Rough ice thickness (h_I) in orange. Vertical dotted lines indicate boundaries identified from aerial photographs (see Figure 3 for transects A–B). Regions outside the fast ice shaded in gray, ice older than 45 days coastward of green arrows. Core lengths of consolidated sea ice (magenta) and with estimates of SIPL (cyan) for January 1994 and October 1995 (Tison et al., 1998).

of the dashed lines in Figure 6a, and a narrow border of multiyear ice (<500 m wide) hugging the eastern coast of the embayment, that survived through summer 2016/2017. This multiyear ice was not surveyed in November 2017.

Our results show that the relatively thin, just over 1 month old, level ice had a mean thickness of 1.1 ± 0.3 m, underlain by a substantial SIPL of thickness 3.4 ± 2.2 m (Figures 6b and 6c). That is, the fast ice grew to about 1.1 m thick in 45 days, implying a spectacularly high average growth rate of 2.5 cm d^{-1}. We surmise that this level ice was protected by the triangular-shaped region of rough ice, and grew rapidly with heat extracted to the atmosphere by katabatic winds and to the ocean by supercooled ISW. Heat fluxes will be estimated in Section 5.

Providing a barrier that protects the level ice, the rough ice was a very thick rubble field (see airborne camera mosaic in Figure 3) deformed by wind-driven compression against the coast. Time series of MODIS images
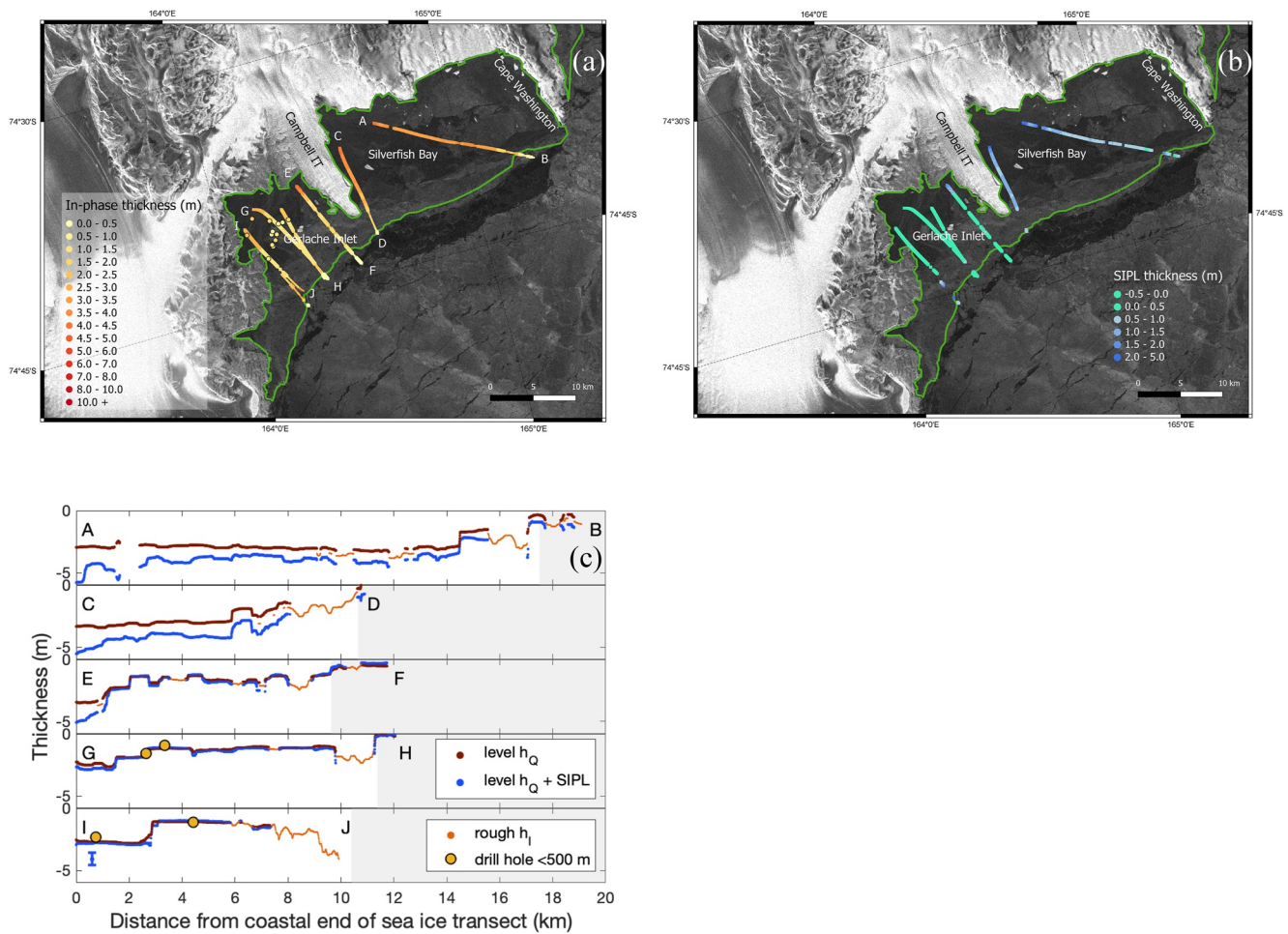
Figure 7. Gerlache Inlet and Silverfish Bay, Terra Nova Bay (a) In-phase apparent thickness (h_I) plotted on Sentinel-1 Interferometric Wide (IW) swath mode image acquired 10 November 2017 10:29 UTC. Locations A–J identified. Level ice shown as thicker line (squares), rough ice as thinner line (circles). Drill hole thickness measurements on level ice shown by larger circles with black rims. Fast ice edge indicated by green line. (b) As (a) but with SIPL thickness under level ice. (c) Five transects bounded by points A–J plotted against distance from coastal end of transect. Thickness measured downwards from snow/ice surface at zero. Consolidated level ice thickness (h_Q) in brown, consolidated ice thickness plus SIPL in blue (uncertainty indicated by bar in panel I–J). Rough ice thickness (h_I) in orange. Orange circular symbols with black rim are drill hole measurements within 500 m of transects. Regions outside fast ice edge shaded gray.

confirm that it formed sometime between 30 September and 5 October (Zhai et al., 2019), during the same coastward deformation event on 4 October reported by Rack et al. (2021). Thus, the rough ice had likely been in place for just over a month at the time of the survey. Its mean thickness was 4.7 ± 0.6 m, with a mode of 4.4 m, in agreement with a single, December 2017, ice-breaker observation of 3–4 m in the vicinity of our location F (Zhai et al., 2019). Unlike the thinner ice toward the ice shelf, this feature was only present four times between 2003 and 2017 (Zhai et al., 2019), and we speculate that it may be related to the increased activity in the Terra Nova Bay polynya, as noted for 2017 by Yoon et al. (2020). The thin ice (mean = 0.3 ± 0.1 m) seaward of the deformed ice in the outer fast ice zone (Figures 6a and 6c) was newly formed nilas ice, as can be seen in Figure 3.

Our airborne measurements agree well with earlier on-ice observations. Tison et al. (1998) reported platelet ice in first-year land-fast sea ice in front of the Hells Gate Ice Shelf in January 1994 and October 1995. There is considerable uncertainty in the relative positions because, in the two decades between the Tison et al. (1998) observations and our AEM surveys, we estimate that the ice shelf front would have advanced ~80 m in the east (A–B in Figure 6c) and 300–400 m in the west (E-F in Figure 6c).

In October 1995, Tison et al. (1998) reported an ice core with a length of 1.35 m in close agreement with the AEM consolidated ice thickness (see middle panel Figure 6c) at a site ~1.2 km along transect C-D. Further, Tison et al. (1998) report "large amounts of loose frazil" beneath the fast ice where our present estimate is an
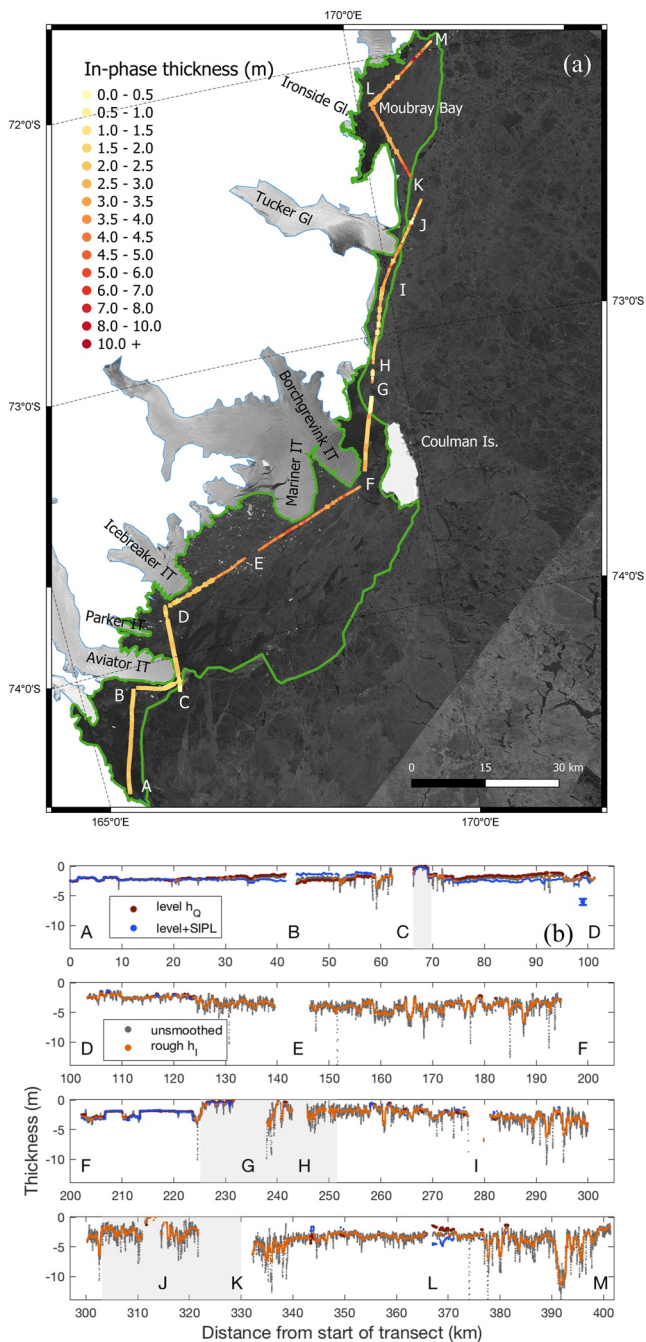
Figure 8. Northern Victoria Land coast (a) In-phase apparent thickness (h_I) plotted on Sentinel-1 Interferometric Wide (IW) swath mode images acquired 19 November 2017 10:05 UTC and 20 November 2017 15:36 UTC. Locations A–M identified. Level ice shown as thicker line (squares), rough ice as thinner line (circles). Fast ice edge indicated by green line. (b) Thickness plotted against distance from beginning of transect, locations A–M identified. Thickness measured downwards from snow/ice surface at zero. Unsmoothed data shown in gray. All other data smoothed with 100-point median filter. Consolidated level ice thickness (h_Q) in brown, consolidated ice thickness plus sub-ice platelet layer (SIPL) in blue (uncertainty indicated by bar in top panel). Rough ice thickness (h_I) in orange. Regions outside the fast ice edge shaded in gray.

SIPL of 2.4 m. In January 1994, Tison et al. (1998) sampled eight core holes from first-year fast ice at a distance of 50–150 m from the ice shelf front. Remarkably, the pattern of platelet ice accumulation along the ice shelf front in spring 2017 concurs with that of Tison et al.'s (1998) summer observations two decades earlier. They report "no significant amount of loose ice crystals" in the section of the transect on the western side of the ice shelf front. This is consistent with an SIPL of less than 1 m between 1 and 2.5 km from the ice shelf front on transect E to F (see bottom panel Figure 6c). In contrast, in the east "a thick layer of about 3–4 m" was observed by Tison et al. (1998), consistent with our SIPL observation beyond 1 km from the ice shelf front of 2.5–5 m from A–B to C–D.

4.2.3. Gerlache Inlet and Silverfish Bay, Terra Nova Bay (TNB)

Seven flight transects (~76 km in total) were conducted over Gerlache Inlet and Silverfish Bay in northern Terra Nova Bay, a sheltered bay in which first-year fast ice forms annually (Figure 2a). Gerlache Inlet is partially separated from Silverfish Bay by the Campbell Glacier Tongue (see Figure 7a), a fast-flowing glacier that is grounded near the ice front at its southwestern end (Han et al., 2022). Ice thickness was measured in 14 drill holes in November 2017 in Gerlache Inlet. Good agreement was found with our in-phase apparent thicknesses h_I (see Figure 7a). No platelet ice was recorded in the drill holes (see Figures 7a and 7c) and the AEM survey confirms SIPL was thin in Gerlache Inlet (see Figure 7b).

This region was ice free in late February/early March 2017 and in-phase apparent thickness, shown in Figure 7a is consistent with thermodynamically grown, 8 months old, first-year fast ice. There are significant portions of level ice (72% of the cover by length) allowing SIPL thickness to be determined (Figure 7b). Here level fast ice had a mean thickness of 2.1 ± 0.8 m. The rough fast ice was only slightly thicker (mean = 2.3 ± 0.7 m) implying that there is relatively little deformed ice or ice older than first-year in the embayment. The 2017 observed median ice thickness of 2.3 m is thinner than median values of Vacchi et al. (2012) in 2005 and 2006, who found consolidated ice median thicknesses from drill holes lay between 2.4 and 2.8 m during surveys for Antarctic silverfish eggs. The discrepancy between 2005/2006 and 2017 thicknesses probably reflects the fact that our survey extended to the fast ice edge, while theirs was concentrated closer to the coast. Figure 7a confirms the increase in sea ice thickness toward the coast. Although no detailed sea ice or SIPL thickness distributions are available, in 2005/2006 the thickest consolidated fast ice consistently appears to be to the east of the Campbell Ice Tongue (Vacchi et al., 2012).

An SIPL was definitively detected by the airborne survey, confirming qualitative observations of the occurrence of platelet ice in 37% of drill holes in 2005 and 88% in 2006 (Vacchi et al., 2012). The consolidated ice thickness and thickness with the SIPL of the five longest transects (~64 km) are shown in Figure 7c. The thickest SIPLs were observed to the east of the Campbell Ice Tongue (in Silverfish Bay and west of Cape Washington) with SIPLs of 2.8 and 2.1 m at A and C, respectively, at the coastal ends of these profiles (see Figures 7b and 7c). On the eastern side of the Campbell Ice Tongue (C-D in Figure 7) the maximum SIPL thickness of 2.1 m decreases to just beneath 1 m about 3 km from the coastal end of the transect. However, this 1 m thick SIPL then persisted along the 8 km surveyed. By contrast on the western side of the Campbell Ice Tongue, in Gerlache Inlet, the SIPL is thinner. Here, the maximum of 1.6 m decreases to less than 0.5 m within 1.2 km (see Figures 7b

and 7c). Perhaps this implies that the Campbell Ice Tongue is the source of supercooled water that is swept eastward by the cyclonic ocean currents (Van Woert et al., 2001; Yoon et al., 2020).

4.2.4. North Victoria Land Coast (NVL)

The transect from Cape Washington to Cape Adare passed some substantial glacier tongues (see Figure 8a), however, the SIPL had a modal thickness of 0 m and a mean of 0.2 ± 0.7 m; the smallest value of any of our selected regions. The level fast ice (see example in Figure S2a in Supporting Information S1) had a mean thickness of 1.9 ± 0.4 m (mode = 1.9 m), thinner than that to the south (mode = 2.0 m). However only 35% of the transect was level ice (Figure 8b). Rough ice occupied 65% of this 400 km stretch of coast by transect length (75% by transect volume) with a mean thickness of 3.3 ± 1.2 m. As a result, the mean thickness of the fast ice (level + rough) was 2.9 ± 1.2 m (see Figures 8a and 8b), the thickest of the four regions identified and thicker than the expected thermodynamic thickness in November, emphasizing the important role of deformation on the fast and pack ice in this region. Indeed a maximum thickness in excess of 11 m was encountered toward the northern end of the transect, where the thickness consistently exceeded 8 m along a 2 km stretch in Moubray Bay (see Figure 8a and section L to M of Figure 8b and photograph of Figure S2b in Supporting Information S1). Inspection of MODIS images suggests that this feature had been incorporated into the fast ice cover for about 7 months and was possibly thick pack ice floes (Rack et al., 2021), or fragments of the previous disintegrating fast ice cover (Hollands & Dierking, 2016).

There was also highly deformed ice between E and F (Figure 8b) with an average thickness of 4.0 m along a 47 km portion of transect. Mobile ice piles up in this region because of the shape of the eastward protruding coastline relative to the generally northward-flowing current.

There is only one short section of this transect where the fast ice was level and where we clearly identified an SIPL with a thickness larger than the uncertainty of ±0.5 m. This was in Moubray Bay, where approx. 4 km of transited level ice at L in Figures 8a and 8b showed an SIPL which decreased in thickness from 3.3 m at the coastal end of the transect close to the floating Ironside Glacier, to 1.6 m at the furthest edge of the level ice.

5. Discussion

5.1. Factors Influencing Fast Ice Thickness in the Western Ross Sea

The region with the greatest climatological rate of decrease in fast ice extent in the Southern Ocean, over 2000–2018, is Victoria and Oates Land (Fraser et al., 2021). While we are unable to identify the processes causing this maximal decrease in fast ice extent, we do provide baseline fast ice thicknesses for, for example, further modeling studies, and attribute factors causing thickness variations in 2017. Our AEM survey flights took place within this region between 8 and 13 November 2017 (DOY = 312–317). This is 30 days later than the maximum in fast ice extent (DOY = 285), and therefore likely to be close to the maximum annual fast ice thickness. Along the Victoria Land Coast, the fast ice is influenced by polynya processes and by Ice Shelf Water generated from interaction with continental ice. Our measurements are only a snapshot in time, but the processes which determine the fast ice thickness recur: that is, multiple polynya events take place every year (Dai et al., 2020; Dale et al., 2017; Tison et al., 2020) while ISW is pervasive from year to year (e.g., Budillon & Spezie, 2000; Langhorne et al., 2015). Thus, our aim in this study is to quantify the relative influence on fast ice thickness of thermodynamic growth (sometimes in the presence of ISW), and of ice deformation (often caused by related polynya activity).

Our survey is approximately north-south covering a latitudinal gradient of just under 6 degrees of latitude (−77.7° to −72.0°; approximately 650 km). While thermodynamically one could expect thinner ice farther to the north, we show that, on average, the thickest fast ice, and significantly thicker than the surveyed pack ice (see Rack et al., 2021 and Figure 4b), is along the northern coastal transect (see Figure 8) from Cape Washington to Cape Adare. We have shown that this is the result of deformation against coastal features, so begin by examining this deformed ice.

5.2. Thickness of Rough Fast Ice

Rough ice constituted 41% of the total fast ice transect length but 50% of its volume. The effect of rough ice is seen in the histogram of 100-point median-filtered, in-phase, apparent thickness for 2017, shown in Figure 1.

The overall result is that, while the modal ice thickness was 2.0 m, the mean of 2.6 ± 1.0 m was higher because of the significant contribution of rough ice to the profiles. In comparison with other years, airborne and satellite altimetry implies that the freeboard of the coastal sea ice of the western Ross Sea in 2017 was greater (and hence the sea ice thicker) than in 2003–2008, and 2016 (Tian et al., 2020). Noting evidence that the TNB polynya was also more active in 2017 than in the early 2000s (Yoon et al., 2020), we conjecture that the fast ice of 2017 may have been thicker because of the multiple polynya events that sculpt the fast ice edge and cause deformation against coastal features.

A correlation between ice thickness and surface roughness has been observed over Arctic fast ice (Beckers et al., 2015). In Antarctic fast ice, Giles et al. (2008) have previously highlighted the contribution of rough ice to the thickness distribution. They classified fast ice in East Antarctica as "smooth" or "rough," based on calibrated radar backscatter images, and found a 2:1 area ratio of smooth to rough fast ice. With the definition of roughness in Section 3.3, our study finds a larger portion of rough ice by length, 3:2, in the western Ross Sea. Further Giles et al. (2008) assigned thicknesses to "smooth" and "rough" fast ice, respectively, of 1.7 and 5.0 m. The mean thicknesses measured in the western Ross Sea in spring are bracketed by these extremes, with 2.0 m for level, and 3.2 m for rough, respectively. We are unable to make further comparison because the rough ice threshold cannot be extended beyond our 1D survey lines to provide areal information.

As discussed in Section 4.2.4, one of the longer stretches of rough ice in our survey, between locations D and F of Figures 8a and 8b (from the Aviator Glacier to the Borchevink Glacier), displayed thicknesses in the range 3–5 m (see 100–200 km of transect of Figure 8b). This coastline was ice free on 17 February 2017, but patches of mobile ice persisted offshore. As shown by Rack et al. (2021), polynya activity in Terra Nova Bay drives ice eastward from the coast, that then drifts north to be trapped and frozen in place against the eastward projection of the coast. It is possible that thick, multiyear ice floes had become frozen within the fast ice cover. The thickest ice of the survey is the rough ice from H and M of Figures 8a and 8b, from north of Coulman Island up to Moubray Bay (see 250–400 km of transect of Figure 8b). Again this ice has been attached to the coast for less than a year, but may be a mélange of thick, old floes.

In order to reliably identify the SIPL, both in-phase and quadrature signals are needed. The quadrature signal has a low signal-to-noise ratio and requires smoothing (as done in most of this work and described in Section 3.2). However, over rough ice, smoothing resulted in reductions of maximum ridge thicknesses which can be seen by comparing smoothed (Figure 4a and Table 1) versus unsmoothed (Figure 4b and Table 2) fast ice statistics. While the overall mean and median values differ by 0.1 m or less between smoothed and unsmoothed data, the mean value of the thickest 10% of fast ice (h_{H10}) is 0.8 m thicker when unsmoothed than when smoothed. Thus, we have underestimated the thickest fast ice by up to 20% because of our need to smooth the data for SIPL detection. In addition, it is well known that the retrieved unsmoothed thickness of unconsolidated ridges may be up to 50% less than the "true" thickness (e.g., Haas & Jochmann, 2003; Pfaffling et al., 2007) because of the footprint of the EM instrument. We conclude that the values reported here of thickest rough fast ice may be only 40% of its "true" thickness. If we had made no attempt to obtain an SIPL thickness, then the in-phase signal alone would have been needed and unsmoothed data used, as we have done for the data presented in Table 2.

5.3. Volume and Influence of the Sub-Ice Platelet Layer Under Level Fast Ice

In order to obtain an overall sense of the contribution of SIPL to the volume of level fast ice, we consider the transect volume of SIPL in comparison to that of consolidated ice plus snow. South of 75°, in New Harbor and Granite Harbor where level ice comprises 76% of the transect volume, the SIPL transect bulk volume is 0.30 times consolidated ice volume, a significant contribution. North of 75°, where only 33% of the volume of the fast ice is level ice, the contribution of the SIPL is 0.25 times consolidated level ice volume, and thus a small fraction of the total volume of ice surveyed to the north of 75°. This emphasizes the dominance of the McMurdo/Ross Ice Shelf in modifying sea ice in the southern Ross Sea. We caution that our observations are biased by the challenges of detecting an SIPL under rougher ice using airborne single-frequency EM techniques (which underestimates SIPL volume), and by the fact that there is a large uncertainty in SIPL thickness, as outlined in Section 3.2.

In spite of the caveats on our observations, ISW is clearly a factor of influence for New Harbor, with 45% of the level ice surveyed having an SIPL greater than 0.5 m. We note that the New Harbor transects close to locations E, G, and I (Figure 5), are in a region where Fraser et al. (2021) has identified fast ice with a mean age of

18–24 months. Indeed, second year ice was observed there in 2017 (Figure 5c) with a thickness of 3–5, hinting that the presence of an SIPL may strongly contribute to the thickness and persistence of the fast ice at this location.

There is one exceptional instance of the influence of ISW; in front of the Hells Gate Ice Shelf where we estimate the heat fluxes associated with the formation of level ice within 3 km of the front of the ice shelf. Our results (Section 4.2.2) show that relatively thin, level ice with a mean thickness of 1.1 ± 0.3 m, underlain by a substantial SIPL of thickness 3.4 ± 2.2 m (Figures 6b and 6c), formed in 45 days, that is, with a growth rate of 2.5 cm d^{-1}. For comparison, Purdie et al. (2006) measured an average growth rate of 1.5 cm d^{-1} in a protected, supercooled bay, some 325 km to the south. We know that, within 5–10 days of the initial formation of the Hells Gate level ice, it became sheltered by the triangular-shaped region of rough ice (Zhai et al., 2019). Held in position, we assume that katabatic winds kept the sea ice surface largely free of snow (supported by the photos in Figure 3), allowing rapid heat transfer to the atmosphere. Heat transfer also took place to the ocean.

We note that sea ice in front of the Hells Gate Ice Shelf in 2017 was of similar thickness to that sampled in 1994/1995, and crystallographic evidence suggests that granular/platelet ice formed throughout the entire sea ice cover (Tison et al., 1998). We therefore conjecture that, over 45 days, heat has been extracted to the ocean to form 4.5 m SIPL, and that 1.1 m of this SIPL became consolidated due to heat flux to the atmosphere. Assuming the SIPL has a solid fraction of 0.25 (Hoppmann et al., 2020), we follow Langhorne et al. (2015) to estimate an average oceanic heat flux of -90 W m^{-2}, during October and within 3 km of the ice shelf front. This value is reasonable for an October average, when the surface ocean of the western Ross Sea is at its coldest (Mahoney et al., 2011), and at such close proximity to the ice shelf. The heat flux to the atmosphere to consolidate the ice cover (i.e., to form 0.75×1.1 m of sea ice) requires an average of 65 W m^{-2}. This is a realistic value (Gough et al., 2012) for fast ice less than 1 m thick with a thin snow cover in an area where there are frequent katabatic wind events driving high turbulent heat fluxes (Tison et al., 1998).

The large volumes of SIPL discussed above are perhaps surprising, so can we justify these? Partly they are a result of flight track limitations, and the focus on the harbor regions, rather than an attempt to conduct an inclusive, representative grid survey that sampled the fast ice types proportionately. Theoretical considerations (Wongpan et al., 2021) have demonstrated that an SIPL grows more rapidly than congelation ice. Its growth rate is linearly related to thermal forcing (as observed by e.g., Smith et al., 2012), rather than a growth rate that decreases with ice thickness as for congelation ice. Thus thick SIPLs may flourish under thick fast ice, explaining the large SIPL thicknesses observed (e.g., Hoppmann et al., 2020; Hughes et al., 2014) and the relatively high SIPL volumes indicated here. The large liquid fraction of the SIPL enhances its stability, in particular by providing a low thermal diffusivity, while convection within the isothermal SIPL does not transport heat. Thus, in spite of the fact that an SIPL provides little extra mechanical strength to the sea ice cover, its thermal properties isolate the base of the sea ice from the ocean below. Since our knowledge of the SIPL is very poor during the decay period (Wongpan et al., 2021), the amount of extra protection provided by an SIPL to the fast ice that fringes continental ice is a key topic of future study.

6. Conclusions

As a baseline for future studies, this first-time inventory of fast ice thickness in the western Ross Sea is the result of a 700 km long airborne electromagnetic (AEM) induction survey in November 2017 over mainly first-year fast ice. The thickness of a sub-ice platelet layer (SIPL) can be estimated under level ice, but not under rough ice, incentivizing the use of a level/rough ice filter. The AEM flights took place approximately 30 days after the maximum in fast ice extent in Victoria and Oates Land, and it is therefore likely that the fast ice was close to its maximum annual thickness. Only in New Harbor had the ice been in place throughout the previous summer. In the following, we address the three questions posed at the end of Section 1:

1. For the fast ice of the Victoria Land coast between New Harbor and Cape Adare, the modal consolidated ice (+snow) thickness was 1.9 m, significantly less than its mean of 2.6 ± 1.0 m. The overall thickness distribution was a superposition of the distribution of level ice (mode = 2.0 m; mean = 2.0 ± 0.6 m) with rough ice (mode = 3.3 m; mean = 3.2 ± 1.2 m). The mean and median of fast ice thicknesses were approx. 0.7 m (~30%–40%) greater than a concurrent survey of pack ice in the same region (Rack et al., 2021), while the mode was more than 1.5 m greater in the fast ice. Thus, while the area covered by land-fast sea ice was only 2% of the total sea ice area in the western Ross Sea in November 2017 (Li et al., 2020), the fast ice contribution to sea ice volume was significant.

2. The fast ice of the western Ross Sea consists of significant proportions (41% by transect length, 50% by transect volume) of rough ice. Deformation is closely linked with polynya activity and multiple such events occur every year, sculpting the fast ice edge. While the modal thicknesses of thermodynamically grown, level ice north of 75°S was 0.1 m thinner than that south of 75°S, overall the northern ice was 0.4 m thicker (2.8 versus 2.4 m) on average because of the higher proportion of rough ice in the north (58% versus 19% by transect length). On average the thickest fast ice lay along the coast from Cape Washington to Cape Adare. This demonstrates that any effect of latitudinal gradient in climate, snow cover, or the presence of ISW, is overwhelmed by ice deformation against coastal features. The thickest 10% of rough fast ice had a mean of almost 6 m, and in Moubray Bay a 2 km long stretch was observed with a thickness in excess of 8 m.

3. The presence of an SIPL, likely due to ISW in the upper surface ocean, was definitively observed in four embayments: the Silverfish Bay region of Terra Nova Bay, offshore Hells Gate Ice Shelf, New Harbor, and Granite Harbor. Beneath level fast ice an SIPL with a mean of 0.6 ± 1.0 m, mode = 0.1 m, existed along the Victoria Land coast. This disguises the fact that in some locations the SIPL was almost 10 m thick, and the thickest 10% had an average thickness of 2.7 m. Indeed, in New and Granite harbors the SIPL transect bulk volume was a significant fraction (0.30) of the consolidated ice volume. We estimate that the sheltered fast ice in front of the Hells Gate Ice Shelf formed with average heat loss to the ocean of 90 W m^{-2} during October, while simultaneous heat loss to the atmosphere implies a vigorous wind-driven component. There were areas where there was a hint of an SIPL beneath level ice, such as close to the Ironside Glacier front in northern Victoria Land. It is very likely that thin SIPLs are more pervasive than implied from our survey because they can only be clearly detected with AEM when their thickness is greater than 0.5 m, and because an SIPL cannot be detected in the presence of heavily deformed ice, with unconsolidated keels, which was abundant in the study region. In addition, our one-dimensional flight tracks still sparsely cover the land-fast ice. Clearly proximity to continental ice, that drives katabatic winds and generates ISW, is a critical factor in governing the thickness of Antarctic fast ice.

Data Availability Statement

The airborne electromagnetic induction data collected in the western Ross Sea in the study are available from Langhorne et al. (2022), https://doi.org/10.1594/PANGAEA.950402. Sentinel-1 SAR images were downloaded from the Alaska SAR Facility Data Search Vertex. https://search.asf.alaska.edu in GRD (ground range detected) format and converted to calibrated backscattering (sigma-0) images in polarstereographic projection using the Gamma Remote Sensing software package.

References

Ainley, D. G., Larue, M. A., Stirling, I., Stammerjohn, S., & Siniff, D. B. (2015). An apparent population decrease, or change in distribution, of Weddell seals along the Victoria Land coast. *Marine Mammal Science*, *31*(4), 1338–1361. https://doi.org/10.1111/mms.12220

Arndt, S., Hoppmann, M., Schmithüsen, H., Fraser, A. D., & Nicolaus, M. (2020). Seasonal and interannual variability of landfast sea ice in Atka Bay, Weddell Sea, Antarctica. *The Cryosphere*, *14*(9), 2775–2793. https://doi.org/10.5194/tc-14-2775-2020

Barry, J. P. (1988). Hydrographic patterns in McMurdo Sound, Antarctica and their relationship to local benthic communities. *Polar Biology*, *8*(5), 377–391. https://doi.org/10.1007/BF00442029

Beckers, J., Renner, A., Spreen, G., Gerland, S., & Haas, C. (2015). Sea-ice surface roughness estimates from airborne laser scanner and laser altimeter observations in Fram Strait and north of Svalbard. *Annals of Glaciology*, *56*(69), 235–244. https://doi.org/10.3189/2015AoG69A717

Bell, R., Chu, W., Kingslake, J., Das, I., Tedesco, M., Tinto, K. J., et al. (2017). Antarctic ice shelf potentially stabilized by export of meltwater in surface river. *Nature*, *544*(7650), 344–348. https://doi.org/10.1038/nature22048

Brett, G. M., Irvin, A., Rack, W., Haas, C., Langhorne, P. J., & Leonard, G. H. (2020). Variability in the distribution of fast ice and the sub-ice platelet layer near McMurdo Ice Shelf. *Journal of Geophysical Research: Oceans*, *125*, e2019JC015678. https://doi.org/10.1029/2019JC015678

Brett, G. M., Price, D., Rack, W., & Langhorne, P. J. (2021). Satellite altimetry detection of ice-shelf-influenced fast ice. *The Cryosphere*, *15*(8), 4099–4115. https://doi.org/10.5194/tc-15-4099-2021

Budillon, G., & Spezie, G. (2000). Thermohaline structure and variability in the Terra Nova bay polynya, Ross Sea. *Antarctic Science*, *12*(4), 493–508. https://doi.org/10.1017/S0954102000000572

Cummings, V. J., Barr, N. G., Budd, R. G., Marriott, P. M., Safi, K. A., & Lohrer, A. M. (2019). In situ response of Antarctic under-ice primary producers to experimentally altered pH. *Scientific Reports*, *9*(1), 6069. https://doi.org/10.1038/s41598-019-42329-0

Currie, A. A., Marshall, A. J., Lohrer, A. M., Cummings, V. J., Seabrook, S., & Cary, S. C. (2021). Sea ice dynamics drive benthic microbial communities in McMurdo Sound, Antarctica. *Frontiers in Microbiology*, *12*, 745915. https://doi.org/10.3389/fmicb.2021.745915

Dai, L., Xie, H., Ackley, S. F., & Mestas-Nuñez, A. M. (2020). Ice production in Ross ice shelf polynyas during 2017–2018 from Sentinel-1 SAR images. *Remote Sensing*, *12*(9), 1484. https://doi.org/10.3390/rs12091484

Dale, E. R., McDonald, A. J., Coggins, J. H. J., & Rack, W. (2017). Atmospheric forcing of sea ice anomalies in the Ross Sea polynya region. *The Cryosphere*, *11*(1), 267–280. https://doi.org/10.5194/tc-11-267-2017

Debenham, F. (1965). The glacier tongues of McMurdo sound. *The Geographical Journal*, *131*(3), 369–371. https://doi.org/10.2307/1794191

Foldvik, A., & Kvinge, T. (1974). Conditional instability of sea-water at freezing-point. *Deep Sea Research*, *21*(3), 69–174. https://doi.org/10.1016/0011-7471(74)90056-4

Foley, N., Tulaczyk, S. M., Grombacher, D., Doran, P. T., Mikucki, J., Myers, K. F., et al. (2019). Evidence for pathways of concentrated submarine groundwater discharge in East Antarctica from helicopter-borne electrical resistivity measurements. *Hydrology*, *6*(2), 54. https://doi.org/10.3390/hydrology6020054

Fons, S. W., & Kurtz, N. T. (2019). Retrieval of snow freeboard of Antarctic sea ice using waveform fitting of CryoSat-2 returns. *The Cryosphere*, *13*(3), 861–878. https://doi.org/10.5194/tc-13-861-2019

Fraser, A. D., Massom, R. A., Handcock, M. S., Reid, P., Ohshima, K. I., Raphael, M. N., et al. (2021). 18 year record of circum-Antarctic landfast sea ice distribution allows detailed baseline characterisation, reveals trends and variability. *The Cryosphere*, *15*(11), 5061–5077. https://doi.org/10.5194/tc-15-5061-2021

Fraser, A. D., Massom, R. A., Ohshima, K. I., Willmes, S., Kappes, P. J., Cartwright, J., & Porter-Smith, R. (2020). High-resolution mapping of circum-Antarctic landfast sea ice distribution, 2000–2018. *Earth System Science Data*, *12*(4), 2987–2999. https://doi.org/10.5194/essd-12-2987-2020

Frezzotti, M. (1997). Ice front fluctuation, iceberg calving flux and mass balance of Victoria Land glaciers. *Antarctic Science*, *9*(1), 61–73. https://doi.org/10.1017/S0954102097000096

Fusco, G., Budillon, G., & Spezie, G. (2009). Surface heat fluxes and thermohaline variability in the Ross Sea and in Terra Nova bay polynya. *Continental Shelf Research*, *29*(15), 1887–1895. https://doi.org/10.1016/j.csr.2009.07.006

Giles, A. B., Massom, R. A., & Lytle, V. I. (2008). Fast-ice distribution in East Antarctica during 1997 and 1999 determined using RADARSAT data. *Journal of Geophysical Research*, *113*, C02S14. https://doi.org/10.1029/2007JC004139

Gomez-Fell, R., Rack, W., Purdie, H., & Marsh, O. (2022). Parker Ice Tongue collapse, Antarctica, triggered by loss of stabilizing landfast sea ice. *Geophysical Research Letters*, *49*, e2021GL096156. https://doi.org/10.1029/2021GL096156

Gough, A., Mahoney, A., Langhorne, P., Williams, M., Robinson, N., & Haskell, T. (2012). Signatures of supercooling: McMurdo sound platelet ice. *Journal of Glaciology*, *58*(207), 38–50. https://doi.org/10.3189/2012JoG10J218

Gow, A. J., Ackley, S. F., Govoni, J. W., & Weeks, W. F. (1998). Physical and structural properties of land-fast sea ice in McMurdo Sound, Antarctica. In M. O. Jeffries (Ed.), *Antarctic Sea ice: Physical processes, interactions and variability, Antarctic Research Series* (Vol. 74, pp. 355–374). American Geophysical Union. https://doi.org/10.1029/AR074p0355

Haas, C. (2004). Airborne EM sea-ice thickness profiling over brackish Baltic sea water. In *Proceedings of the 17th international IAHR symposium on ice, June 21–25, 2004, St. Petersburg, Russia* (Vol. 2, pp. 12–17). All-Russian Research Institute of Hydraulic Engineering (VNIIG).

Haas, C. (2006). Airborne electromagnetic sea ice thickness sounding in shallow, brackish water environments of the Caspian and Baltic Seas. In *Proceedings of OMAE2006 25th international conference on offshore mechanics and Arctic engineering*. The American Society of Mechanical Engineers.

Haas, C., Hendricks, S., Eicken, H., & Herber, A. (2010). Synoptic airborne thickness surveys reveal state of Arctic sea ice cover. *Geophysical Research Letters*, *37*, L09501. https://doi.org/10.1029/2010GL042652

Haas, C., & Jochmann, P. (2003). Continuous EM and ULS thickness profiling in support of ice force measurements. In S. Loeset, B. Bonnemaire, & M. Bjerkas (Eds.). *Proceedings of the 17th international conference on port and ocean engineering under Arctic Conditions POAC'03, Trondheim, Norway* (Vol. 3, pp. 849–856). Department of Civil and Transport Engineering, Norwegian University of Science.

Haas, C., Langhorne, P. J., Rack, W., Leonard, G. H., Brett, G. M., Price, D., et al. (2021). Airborne mapping of the sub-ice platelet layer under fast ice in McMurdo Sound, Antarctica. *The Cryosphere*, *15*(1), 247–264. https://doi.org/10.5194/tc-15-247-2021

Haas, C., Lobach, J., Hendricks, S., Rabenstein, L., & Pfaffling, A. (2009). Helicopter-borne measurements of sea ice thickness, using a small and lightweight, digital EM system. *Journal of Applied Geophysics*, *67*(3), 234–241. https://doi.org/10.1016/j.jappgeo.2008.05.005

Han, H., Kim, S. H., & Kim, S. (2022). Decadal changes of Campbell Glacier Tongue in East Antarctica from 2010 to 2020 and implications of ice pinning conditions analyzed by optical and SAR datasets. *GIScience & Remote Sensing*, *59*(1), 705–721. https://doi.org/10.1080/15481603.2022.2055380

Han, H., & Lee, H. (2018). Glacial and tidal strain of landfast sea ice in Terra Nova Bay, East Antarctica, observed by interferometric SAR techniques. *Remote Sensing of Environment*, *209*, 41–51. https://doi.org/10.1016/j.rse.2018.02.033

Hellmer, H. H. (2004). Impact of Antarctic ice shelf basal melting on sea ice and deep ocean properties. *Geophysical Research Letters*, *31*, L10307. https://doi.org/10.1029/2004GL019506

Hollands, T., & Dierking, W. (2016). Dynamics of the Terra Nova Bay polynya: The potential of multi-sensor observations. *Remote Sensing of Environment*, *187*, 30–48. https://doi.org/10.1016/j.rse.2016.10.003

Hoppmann, M., Richter, M., Smith, I., Jendersie, S., Langhorne, P., Thomas, D., & Dieckmann, G. (2020). Platelet ice, the Southern Ocean's hidden ice: A review. *Annals of Glaciology*, *61*(83), 1–28. https://doi.org/10.1017/aog.2020.54

Hughes, K. G., Langhorne, P. J., Leonard, G. H., & Stevens, C. L. (2014). Extension of an Ice Shelf Water plume model beneath sea ice with application in McMurdo Sound, Antarctica. *Journal of Geophysical Research: Oceans*, *119*, 8662–8687. https://doi.org/10.1002/2013JC009411

Hunkeler, P. A., Hoppmann, M., Hendricks, S., Kalscheuer, T., & Gerdes, R. (2015). A glimpse beneath Antarctic sea ice: Platelet layer volume from multifrequency electromagnetic induction sounding. *Geophysical Research Letters*, *43*, 222–231. https://doi.org/10.1002/2015GL065074

Jacobs, S. S., Fairbanks, R. G., & Horibe, Y. (1985). Origin and evolution of water masses near the Antarctic continental margin: Evidence from $H^{18}O/H^{16}O$ ratios in seawater. In S. S. Jacobs (Ed.), *Oceanology of the Antarctic continental shelf* (p. 22). American Geophysical Union. https://doi.org/10.1029/AR043p0059

Jeffries, M. O., Weeks, W. F., Shaw, R., & Morris, K. (1993). Structural characteristics of congelation and platelet ice and their role in the development of Antarctic land-fast sea ice. *Journal of Glaciology*, *39*(132), 223–238. https://doi.org/10.1017/s0022143000015884

Jendersie, S., Williams, M. J. M., Langhorne, P. J., & Robertson, R. (2018). The density-driven winter intensification of the Ross Sea circulation. *Journal of Geophysical Research: Oceans*, *123*, 7702–7724. https://doi.org/10.1029/2018JC013965

Jenouvrier, S., Che-Castaldo, J., Wolf, S., Holland, M., Labrousse, S., LaRue, M., et al. (2021). The call of the emperor penguin: Legal responses to species threatened by climate change. *Global Change Biology*, *27*(20), 5008–5029. https://doi.org/10.1111/gcb.15806

Kacimi, S., & Kwok, R. (2020). The Antarctic sea ice cover from ICESat-2 and CryoSat-2: Freeboard, snow depth, and ice thickness. *The Cryosphere*, *14*(12), 4453–4474. https://doi.org/10.5194/tc-14-4453-2020

Kusahara, K., & Hasumi, H. (2014). Pathways of basal meltwater from Antarctic ice shelves: A model study. *Journal of Geophysical Research: Oceans*, *119*, 5690–5704. https://doi.org/10.1002/2014JC009915

Langhorne, P. J., Haas, C., Rack, W., Leonard, G. H., Brett, G. M., & Price, D. (2022). Coastal and landfast sea ice thickness in Western Ross Sea, Antarctica, from airborne electromagnetic induction in November 2017. *PANGAEA*, https://doi.org/10.1594/PANGAEA.950402

Langhorne, P. J., Hughes, K. G., Gough, A. J., Smith, I. J., Williams, M. J. M., Robinson, N. J., et al. (2015). Observed platelet ice distributions in Antarctic sea ice: An index for ocean-ice shelf heat flux. *Geophysical Research Letters*, *42*, 5442–5451. https://doi.org/10.1002/2015GL064508

Leonard, G. H., Purdie, C. R., Langhorne, P. J., Haskell, T. G., Williams, M. J. M., & Frew, R. D. (2006). Observations of platelet ice growth and oceanographic conditions during the winter of 2003 in McMurdo Sound, Antarctica. *Journal of Geophysical Research*, *111*, C04012. https://doi.org/10.1029/2005JCC002952

Leonard, G. H., Turner, K. E., Richter, M. E., Whittaker, M. S., & Smith, I. J. (2021). Brief communication: The anomalous winter 2019 sea-ice conditions in McMurdo Sound, Antarctica. *The Cryosphere*, *15*(10), 4999–5006. https://doi.org/10.5194/tc-15-4999-2021

Lewis, E. L., & Perkin, R. G. (1985). The winter oceanography of McMurdo Sound, Antarctica. In S. S. Jacobs (Ed.), *Oceanology of the Antarctic continental shelf, Antarctic Research Series* (pp. 145–165). American Geophysical Union.

Li, X., Shokr, M., Hui, F., Chi, Z., Heil, P., Chen, Z., et al. (2020). The spatio-temporal patterns of landfast ice in Antarctica during 2006–2011 and 2016–2017 using high-resolution SAR imagery. *Remote Sensing of Environment*, *242*, 111736. https://doi.org/10.1016/j.rse.2020.111736

Mager, S. M., Smith, I. J., Kempema, E. W., Thomson, B. J., & Leonard, G. H. (2013). Anchor ice in polar oceans. *Progress in Physical Geography: Earth and Environment*, *37*(4), 468–483. https://doi.org/10.1177/0309133313479815

Mahoney, A. R., Gough, A. J., Langhorne, P. J., Robinson, N. J., Stevens, C. L., Williams, M. J. M., & Haskell, T. G. (2011). The seasonal appearance of ice shelf water in coastal Antarctica and its effect on sea ice growth. *Journal of Geophysical Research*, *116*, C11032. https://doi.org/10.1029/2011JC007060

Massom, R., Hill, K., Lytle, V., Worby, A., Paget, M., & Allison, I. (2001). Effects of regional fast-ice and iceberg distributions on the behaviour of the Mertz Glacier polynya, East Antarctica. *Annals of Glaciology*, *33*, 391–398. https://doi.org/10.3189/172756401781818518

Massom, R. A., Scambos, T. A., Bennetts, L. G., Reid, P., Squire, V. A., & Stammerjohn, S. E. (2018). Antarctic ice shelf disintegration triggered by sea ice loss and ocean swell. *Nature*, *558*(7710), 383–389. https://doi.org/10.1038/s41586-018-0212-1

McPhee, M. G., Stevens, C. L., Smith, I. J., & Robinson, N. J. (2016). Turbulent heat transfer as a control of platelet ice growth in supercooled under-ice ocean boundary layers. *Ocean Science*, *12*(2), 507–515. https://doi.org/10.5194/os-12-507-2016

Meiners, K. M., Vancoppenolle, M., Carnat, G., Castellani, G., Delille, B., Delille, D., et al. (2018). Chlorophyll-a in Antarctic landfast sea ice: A first synthesis of historical ice core data. *Journal of Geophysical Research: Oceans*, *123*, 8444–8459. https://doi.org/10.1029/2018JC014245

Mezgec, K., Stenni, B., Crosta, X., Masson-Delmotte, V., Baroni, C., Braida, M., et al. (2017). Holocene sea ice variability driven by wind and polynya efficiency in the Ross Sea. *Nature Communications*, *8*(1), 1334. https://doi.org/10.1038/s41467-017-01455-x

Moreçki, V. N. (1965). Underwater sea ice. *Probl. Arkt. Antarkt.*, *19*, 32–38. (English translation by E. R. Hope, DRB Canada Rep. No. T497R April, 1968).

Murray, K. T., Miller, M. F., & Bowser, S. S. (2013). Depositional processes beneath coastal multi-year sea ice. *Sedimentology*, *60*(2), 391–410. https://doi.org/10.1111/j.1365-3091.2012.01345.x

Nakata, K., Ohshima, K. I., & Nihashi, S. (2021). Mapping of active frazil for Antarctic coastal polynyas, with an estimation of sea-ice production. *Geophysical Research Letters*, *48*, e2020GL091353. https://doi.org/10.1029/2020GL091353

Nihashi, S., & Ohshima, K. I. (2015). Circumpolar mapping of Antarctic coastal polynyas and landfast sea ice: Relationship and variability. *Journal of Climate*, *28*(9), 3650–3670. https://doi.org/10.1175/JCLI-D-14-00369.1

Pfaffling, A., Haas, C., & Reid, J. E. (2007). Direct helicopter EM—Sea-ice thickness inversion assessed with synthetic and field data. *Geophysics*, *72*(4), F127–F137. https://doi.org/10.1190/1.2732551

Price, D., Beckers, J., Ricker, R., Kurtz, N., Rack, W., Haas, C., et al. (2015). Evaluation of CryoSat-2 derived sea ice freeboard over fast ice in McMurdo Sound, Antarctica. *Journal of Glaciology*, *61*(226), 285–300. https://doi.org/10.3189/2015JoG14J157

Price, D., Rack, W., Haas, C., Langhorne, P. J., & Marsh, O. (2013). Sea ice freeboard in McMurdo Sound, Antarctica, derived by surface-validated ICESat laser altimeter data. *Journal of Geophysical Research: Oceans*, *118*, 3634–3650. https://doi.org/10.1002/jgrc.20266

Price, D., Rack, W., Langhorne, P. J., Haas, C., Leonard, G. H., & Barnsdale, K. (2014). The sub-ice platelet layer and its influence on freeboard to thickness conversion of Antarctic sea ice. *The Cryosphere*, *8*(3), 1031–1039. https://doi.org/10.5194/tc-8-1031-2014

Price, D., Soltanzadeh, I., Rack, W., & Dale, E. (2019). Snow-driven uncertainty in CryoSat-2-derived Antarctic sea ice thickness—Insights from McMurdo Sound. *The Cryosphere*, *13*(4), 1409–1422. https://doi.org/10.5194/tc-13-1409-2019

Purdie, C., Langhorne, P., Leonard, G., & Haskell, T. (2006). Growth of first-year landfast Antarctic sea ice determined from winter temperature measurements. *Annals of Glaciology*, *44*, 170–176. https://doi.org/10.3189/172756406781811853

Rabenstein, L., Hendricks, S., Martin, T., Pfaffhuber, A., & Haas, C. (2010). Thickness and surface-properties of different sea-ice regimes within the Arctic Trans Polar Drift: Data from summers 2001, 2004 and 2007. *Journal of Geophysical Research*, *115*, C12059. https://doi.org/10.1029/2009JC005846

Rack, W., Haas, C., & Langhorne, P. J. (2013). Airborne thickness and freeboard measurements over the McMurdo Ice Shelf, Antarctica, and implications for ice density. *Journal of Geophysical Research: Oceans*, *118*, 5899–5907. https://doi.org/10.1002/2013JC009084

Rack, W., Price, D., Haas, C., Langhorne, P. J., & Leonard, G. H. (2021). sea ice thickness in the Western Ross Sea. *Geophysical Research Letters*, *48*, e2020GL090866. https://doi.org/10.1029/2020GL090866

Robinson, N. J., Williams, M. J. M., Stevens, C. L., Langhorne, P. J., & Haskell, T. G. (2014). Evolution of a supercooled Ice Shelf Water plume with an actively-growing sub-ice platelet matrix. *Journal of Geophysical Research: Oceans*, *119*, 3425–3446. https://doi.org/10.1002/2013JC009399

Rossiter, J. R., & Holladay, J. S. (1994). Ice-thickness measurement. In S. Haykin, E. O. Lewis, R. K. Rainey, & J. R. Rossiter (Eds.), *Remote sensing of sea ice and icebergs* (pp. 141–176). John Wiley and Sons Inc.

Smith, I. J., Langhorne, P. J., Frew, R. D., Vennell, R., & Haskell, T. G. (2012). Sea ice growth rates near ice shelves. *Cold Regions Science and Technology*, *83–84*, 57–70. https://doi.org/10.1016/j.coldregions.2012.06.005

SooHoo, J. B., Palmisano, A. C., Kottmeier, S. T., Lizzotte, M. P., SooHoo, S. L., & Sullivan, C. W. (1987). Spectral light absorption and quantum yield of photosynthesis in sea ice microalgae and a bloom of *Phaeocystis pouchetii* from McMurdo Sound, Antarctica. *Marine Ecology Progress Series*, *39*, 175–189. https://doi.org/10.3354/meps039175

Souchez, R., Meneghel, M., Tison, J. L., Lorrain, R., Ronveaux, D., Baroni, C., et al. (1991). Ice composition evidence of marine-ice transfer along the bottom of a small Antarctic ice shelf. *Geophysical Research Letters*, *18*, 849–852. https://doi.org/10.1029/91GL01077

Stevens, C. L., McPhee, M. G., Forrest, A. L., Leonard, G. H., Stanton, T., & Haskell, T. G. (2014). The influence of an Antarctic glacier tongue on near-field ocean circulation and mixing. *Journal of Geophysical Research: Oceans*, *119*, 2344–2362. https://doi.org/10.1002/2013JC009070

Stevens, C., Sang Lee, W., Fusco, G., Yun, S., Grant, B., Robinson, N., & Yeon Hwang, C. (2017). The influence of the Drygalski Ice Tongue on the local ocean. *Annals of Glaciology*, *58*(74), 51–59. https://doi.org/10.1017/aog.2017.4

Stevens, C. L., Sirguey, P., Leonard, G. H., & Haskell, T. G. (2013). Brief communication "the 2013 Erebus Glacier Tongue calving event". *The Cryosphere*, *7*(5), 1333–1337. https://doi.org/10.5194/tc-7-1333-2013

Stockton, W. (1983). Submarine ice cliffs on the west side of McMurdo Sound, Antarctica. *Journal of Glaciology*, *29*(102), 272–282. https://doi.org/10.3189/S0022143000008327

Tamura, T., Ohshima, K. I., Fraser, A. D., & Williams, G. D. (2016). Sea ice production variability in Antarctic coastal polynyas. *Journal of Geophysical Research: Oceans*, *121*, 2967–2979. https://doi.org/10.1002/2015JC011537

Tian, L., Xie, H., Ackley, S. F., Tinto, K. J., Bell, R. E., Zappa, C. J., et al. (2020). Sea ice freeboard in the Ross Sea from airborne altimetry IcePod 2016–2017 and a comparison with IceBridge 2013 and ICESat 2003–2008. *Remote Sensing*, *12*(14), 2226. https://doi.org/10.3390/rs12142226

Tin, T., & Jeffries, M. (2001). Sea-ice thickness and roughness in the Ross Sea, Antarctica. *Annals of Glaciology*, *33*, 187–193. https://doi.org/10.3189/172756401781818770

Tison, J.-L., Lorrain, R. D., Bouzette, A., Dini, M., Bondesan, A., & Stievenard, M. (1998). Linking landfast sea ice variability to marine ice accretion at Hells Gate Ice Shelf, Ross Sea. In *Antarctic sea ice: Physical processes, interactions and variability* (pp. 375–407). American Geophysical Union.

Tison, J., Maksym, T., Fraser, A., Corkill, M., Kimura, N., Nosaka, Y., et al. (2020). Physical and biological properties of early winter Antarctic sea ice in the Ross Sea. *Annals of Glaciology*, *61*(83), 241–259. https://doi.org/10.1017/aog.2020.43

Vacchi, M., DeVries, A. L., Evans, C. W., Bottaro, M., Ghigliotti, L., Cutroneo, L., & Pisano, E. (2012). A nursery area for the Antarctic silverfish *Pleuragramma antarcticum* at Terra Nova bay (Ross Sea): First estimate of distribution and abundance of eggs and larvae under the seasonal sea-ice. *Polar Biology*, *35*(10), 1573–1585. https://doi.org/10.1007/s00300-012-1199-y

Van Woert, M., Meier, W., Zou, C., Archer, A., Pellegrini, A., Grigioni, P., & Bertoia, C. (2001). Satellite observations of upper-ocean currents in Terra Nova bay, Antarctica. *Annals of Glaciology*, *33*, 407–412. https://doi.org/10.3189/172756401781818879

von Albedyll, L., Haas, C., & Dierking, W. (2021). Linking sea ice deformation to ice thickness redistribution using high-resolution satellite and airborne observations. *The Cryosphere*, *15*(5), 2167–2186. https://doi.org/10.5194/tc-15-2167-2021

Wadhams, P., & Horne, R. (1980). An analysis of ice profiles obtained by submarine Sonar in the Beaufort sea. *Journal of Glaciology*, *25*(93), 401–424. https://doi.org/10.3189/S0022143000015264

Wongpan, P., Vancoppenolle, M., Langhorne, P. J., Smith, I. J., Madec, G., Gough, A. J., et al. (2021). Sub-ice platelet layer physics: Insights from a mushy-layer sea ice model. *Journal of Geophysical Research: Oceans*, *126*, e2019JC015918. https://doi.org/10.1029/2019JC015918

Yoon, S.-T., Lee, W. S., Stevens, C., Jendersie, S., Nam, S. H., Yun, S., et al. (2020). Variability in high-salinity shelf water production in the Terra Nova Bay polynya, Antarctica. *Ocean Science*, *16*(2), 373–388. https://doi.org/10.5194/os-16-373-2020

Zhai, M., Zhao, T., Hui, F., Cheng, X., Liu, A., Yuan, J., et al. (2019). Anomalous extensive landfast sea ice in the vicinity of Inexpressible Island, Antarctica. *Advances in Polar Science*, *30*(4), 406–411. https://doi.org/10.13679/j.advps.2018.0044